IMPROVING THE CORROSION RESISTANCE OF STAINLESS STEEL

by

Stefan Juckes

Submitted in partial fulfilment of the requirements
for the degree of Master of Science

at

Dalhousie University
Halifax, NS
August 2018

TABLE OF CONTENTS

LIST OF TABLES

LIST OF FIGURES

ABSTRACT

Stainless steels are widely used in the food and medical industries. Despite their good corrosion resistance, highly corrosive environments can still lead to material failure. This work investigated the effectiveness of low cost and environmentally friendly surface treatments to improve the corrosion resistance of SS316. Mechanically polished samples were treated by heating in deionized water, a hydrogen peroxide solution, electropolishing and heat treating in an oven. Cyclic voltammetry and optical microscopy were used to measure and image corrosion on the samples in a 0.9% NaCl solution. X-ray photoelectron spectroscopy and ellipsometry were subsequently used to analyze the composition and thickness of the oxide layer. The greatest improvement in corrosion resistance was observed after treating stainless steel in a hydrogen peroxide solution. However, electropolishing also showed a large improvement while having other practical advantages.

LIST OF ABBREVIATIONS AND SYMBOLS USED

λ	Wavelength
ϕ	Work function
AFM	Atomic Force Microscopy
Ag/AgCl	Silver-Silver Chloride Reference Electrode
AISI	American Iron and Steel Institute
Al	Aluminum
CASA	XPS fitting software
CCD	Charge coupled device
Cl^-	Chloride ion
Cr(0)	Chromium metal
Cr_2O_3	Chromium (III) oxide
Cr2p	Chromium 2p peak
Cr	Chromium
$Cr(OH)_3$	Chromium hydroxide
CrS	Chromium sulfide
d	Optical resolution
E_b	Binding energy
EDS	Energy dispersive spectroscopy
E_k	Kinetic energy
Fe_3O_4	Iron (II, III) oxide, also known as magnetite
Fe	Iron

FeO	Iron oxide
FeS	Iron sulfide
$h\nu$	Initial photon energy in x-ray photoelectron spectroscopy
IMFP	Inelastic mean free path
$K\alpha$	X-ray radiation caused by a 2p to 1s electron transition
LED	Light emitting diode
MnS	Manganese sulfide
Mo^{6+}	Molybdenum cation
Mo	Molybdenum
MoO_4^{2-}	Molybdate ion
NaCl	Sodium chloride
Ni	Nickel
NiO	Nickel oxide
NIST	National Institute of Standards and Technology
$nsin\theta$	Numerical aperture
O1s	Oxygen 1s peak
O^{2-}	Oxide ion
OCP	Open circuit potential
pH	Measure of acidity, defined as the negative logarithm of the hydrogen ion concentration
rpm	Revolutions per minute
SEI	Secondary electrons created by primary electrons interacting with the sample

SEII	Secondary electrons created by backscattered electrons interacting with the sample
SEIII	Secondary electrons created by backscattered electrons interacting with material outside the sample
SEM	Scanning Electron Microscope
SHE	Standard Hydrogen Electrode
SiC	Silicon carbide
SS304	Austenitic stainless steel, similar to SS316 but without added molybdenum
SS316	Austenitic stainless steel that is the main focus of this work
TEM	Transmission Electron Microscopy
V_{OCP}	Open circuit potential
V_{pit}	Critical pitting potential
XPS	X-Ray Photoelectron Spectroscopy

ACKNOWLEDGMENTS

This work would not have been possible without the able guidance of my supervisor Dr. Harm Rotermund or the support of my family. I would also like to thank Dr. Mary Anne White for sparking my interest in materials science and helping to improve my writing. Fellow group members Garrett LeGallais and Eduardo Machado provided very useful discussion, feedback and technical help.

Andrew George performed x-ray photoelectron spectroscopy measurements, helped with scanning electron microscopy and also performed the heat treatment of samples for me. Several components of the experimental apparatus were made in the machine shop, by Kevin Borgel and John Noddin. Leah Ellis performed ellipsometry measurements and fitting for me as well. Distilled and deionized water were provided by Dr. Jeff Dahn's lab.

CHAPTER 1: INTRODUCTION

Stainless steels are widely used around the world in everyday applications such as cutlery and food preparation, as well as more specialized applications such as nuclear power plants and medical instruments or implants. This work will look at the efficacy of four different chemical surface treatments to improve the corrosion resistance of SS316 (a widely used grade of austenitic stainless steel). Two of these treatments, using deionized water and hydrogen peroxide, are of particular interest because they are both low cost and environmentally friendly. The methodology used in this testing involved simultaneous pseudo-potentiostatic measurements and microscopic imaging of stainless steel plates immersed in an aqueous solution of sodium chloride (NaCl).

Scanning electron microscope (SEM) and x-ray photoelectron spectroscopy (XPS) measurements were also used to measure the morphology of corrosion pits and chemical composition of the oxide layer respectively. The oxide layer's thickness was measured using ellipsometry.

1.1 History of Stainless Steels

Iron (Fe) is an extremely abundant and versatile element that has been used by humanity both as a pure metal and as steel, when alloyed with carbon, for millennia. However, raw iron and carbon steels both oxidize readily. Particularly in wet or corrosive environments these materials will eventually be destroyed by corrosion. The idea of alloying chromium (Cr) with iron to make corrosion resistant alloys was mentioned as

1

early as 1821, by Berthier [1,2]. Chromium was alloyed with steel used for construction as early as 1869, when constructing the Eads Bridge [2]. The first recognizable modern stainless steels were developed independently by researchers in Germany, the United States and the United Kingdom at the beginning of the 20th century [1,3]. The alloy developed in the United Kingdom by the Brown Firth Research Laboratories was an early martensitic stainless steel [2]. The German alloy, developed by Krupp, was an austenitic stainless steel similar to modern SS304 [2]. The American alloy, developed by Christian Dantsizen in New York was a type of ferritic stainless steel [2]. Stainless steels derive their corrosion resistance from a thin and self-healing passive oxide layer, which is caused by the addition of chromium [4]. Early applications for stainless steels were in cutlery, non-oxidizing wires in lightbulbs and airplane parts during World War I [2].

Initially only martensitic stainless steels were called stainless steel, because of their ability to be hardened by heat treatment. Austenitic and ferritic stainless steels are much more malleable due to their different crystal structures, so they were initially called "alloys" or "stainless iron" to differentiate them from harder steels. The German austenitic stainless steel was marketed under the brand name "Nirosta" which is an abbreviation of nonrusting steel in German [2]. The first use of austenitic stainless steel for medical implants was in 1926 [2]. Duplex stainless steels, which are a combination of austenitic and ferritic structure, were developed in the 1930s [3].

By the 1950s many of the common grades used today had been standardized and industry focus shifted to making these materials at a lower cost. A key advantage of ferritic stainless steels is the relatively low nickel content, which substantially reduces the cost. In addition, the advent of argon-oxygen decarburization marked a significant leap

forward by allowing much lower carbon content in stainless steels [3]. More recently in the 1980s and 1990s "super" alloys have been developed which tend to have higher molybdenum content for significantly increased corrosion resistance.

1.2 Different Types of Stainless Steels

As mentioned in the previous section there are four main families of stainless steels: ferritic, martensitic, austenitic (the subject of this work) and duplex stainless steels. They differ primarily in their crystal structure and have a wide range of physical properties. Austenite has a face centered cubic structure, martensite has a body centered tetragonal structure and ferrite has a body centered cubic structure [5]. In normal carbon steels austenite is not present at room temperature, but the addition of manganese and nickel make it stable at room temperature in stainless steels [5].

Generally austenitic stainless steels have the best corrosion resistance, whereas martensitic stainless steels have superior characteristics for machining and can be hardened by heat treatment. Ferritic stainless steels are a middle ground between austenitic and martensitic in that they can be hardened by heat treatment, but not to the same degree as martensitic stainless steels [2]. Duplex stainless steels have a combination of austenitic and ferritic structure, giving them some of the benefits of both types of stainless steels [1].

The standard naming of stainless steels was first formalized in the 1930s by the American Iron and Steel Institute (AISI) [2]. Stainless steels use a three-number naming system with the first number designating the general family the alloy belongs to and the

3

remaining two being chosen arbitrarily to identify the alloy. Specifically, 3xx is used for austenitic alloys, 4xx for ferritic and martensitic alloys, 5xx for low chromium alloys, 2xx for high manganese alloys and 6xx for proprietary alloys. AISI standard numbering was discontinued in 1960, but the numbers previously assigned are still used for those alloys [2]. In this work alloys will be referred to using their AISI number with the prefix SS (short for stainless steel). Another commonly used nomenclature is of the form 18-10, where 18 refers to the amount of chromium present and 10 refers to the amount of nickel present, in this example 18-10 would be an alternative name for SS304.

This work looked at corrosion on samples of SS316, a high performance austenitic stainless steel. Its composition is shown in Table 1-1 as well as the composition of its sister alloy, SS304. As can be seen from Table 1-1 the only major difference between SS304 and SS316 is the addition of molybdenum, which is added to improve the steel's resistance to corrosion from chloride ions (Cl^-).

Table 1-1:   Approximate compositions of SS316 and SS304. The largest differences are the addition of molybdenum (Mo) in SS316, for enhanced chloride (Cl^-) corrosion resistance and a larger proportion of nickel (Ni). SS304 is the cheaper material used in less corrosive environments [4].

	Cr	Ni	Mo	Fe	C	Mn
SS316	16-18	10-14	2-3	Balance	0.08	2.0
SS304	18-20	8-10	None	Balance	0.08	2.0

1.3 Description of the Oxide Layer

Stainless steels possess a thin and self-repairing oxide layer that leads to a high degree of corrosion resistance. Pure iron corrodes quickly because its oxide layer is thick and will continue to grow until it cracks or becomes porous, exposing fresh material. This process forms rust which is both aesthetically unattractive as well as dangerous for many applications. In medical applications rust can create areas for bacteria to grow and in engineering applications rust can lead to structural failure. Stainless steel uses the addition of chromium and nickel to make a much thinner and stable oxide layer. More advanced stainless steels, such as super-austenitic stainless steels, will add Mo to further enhance corrosion resistance, particularly against aggressive ions such as Cl^- [4]. Stainless steel oxide layers show much higher proportions of Cr and Ni relative to the bulk, with greatly reduced Fe content [6]. They tend to have thicknesses on the order of several nm [4], but this value can vary dramatically depending on surface treatment [4,6,7].

The primary chemical species expected are oxides of chromium (primarily Cr_2O_3), iron (FeO and Fe_3O_4) and nickel (NiO). Some hydroxides may also be present such as $Cr(OH)_3$ [7,8]. A common impurity in steel is sulfur, which is introduced during the manufacturing process from iron ore and coal/coke. Sulfur is generally considered an unwanted impurity. For this reason most steelmakers aim to minimize the sulfur content. However, sulfur does positively affect a steel's machinability so a small amount can be beneficial depending on the application [9,10]. Sulfur forms sulfide deposits in the oxide layer. If the steel is low in manganese (Mn) these deposits can be iron sulfide (FeS) or

chromium sulfide (CrS). However, SS316 has a significant amount of Mn added to encourage the formation of manganese sulfide (MnS) deposits which are more chemically stable and to improve the solubility of nitrogen [11,12].

1.4 Corrosion Mechanisms

Corrosion can be initiated through many different mechanisms. Crevice corrosion is a common and visible type. It often occurs around fasteners, under sediment or near welds and is caused by narrow crevices which lead to an anoxic environment due to oxygen not being able to diffuse through the crevice. Low oxygen in turn leads to a lowered pH due to the reaction shown below [4].

$$O_2 + 2H_2O + 4e^- \rightarrow 4OH^- \tag{1}$$
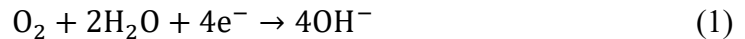
As the environment in the crevice becomes more acidic the energetic barrier to corrosion is reduced leading to large amounts of corrosion.

Crevice corrosion can be minimized by good design, quality control on welds and physical coverage of vulnerable areas by sealants such as paint. This work focussed on pitting corrosion, a subtler form of corrosion whereby corrosion pits form in the oxide layer. These microscopic pits can lead to stress fracturing, but due to their microscopic nature are much harder to observe. Pits generally initiate around a weakness in the oxide layer, such as scratches or inclusions [4]. This is illustrated in Figure 1-1 for scratches in the oxide layer of an SS316 sample measured in this work. On this sample pits preferentially formed along scratches left in the oxide layer during polishing.
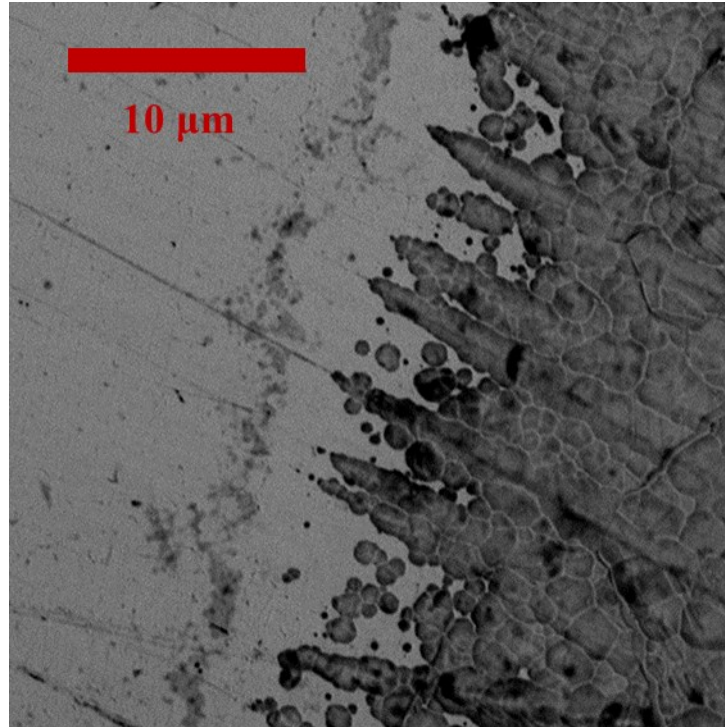
Figure 1-1:   SEM image of corrosion pits following scratches in the oxide layer of an SS316 sample.

There are several proposed mechanisms for the initiation of pitting corrosion: the penetration mechanism, film thinning mechanism and film rupture mechanism. Each will be described separately. In the penetration mechanism, anions (usually chloride ions, Cl^-) are transported through the oxide layer in vacancies in the crystal lattice left from missing oxygen atoms. Chloride ions outperform other electronegative ions, such as bromine or iodine, due to their smaller ionic radius which makes it easier to penetrate the oxide layer [13]. They are also abundant in the environment, making their role in corrosion very widespread and relevant. Once the chloride ions reach the metal surface they can preferentially dissolve the metal. Dissolution and oxide formation form a redox cycle, where metal ions that are being oxidized (losing electrons) are dissolving and metal ions

7

being reduced form an oxide layer (gaining electrons from bonding to oxygen) Figure 1-2 [4].

The film thinning mechanism is similar, but instead of transporting ions through the oxide layer, the oxide layer itself is dissolved. This gradual thinning eventually exposes unprotected metal which will form corrosion pits. The rupture mechanism causes corrosion around imperfections in the oxide layer such as grain boundaries, impurities or inclusions. As an example, the corrosion shown in Figure 1-1 is likely caused by the rupture mechanism.
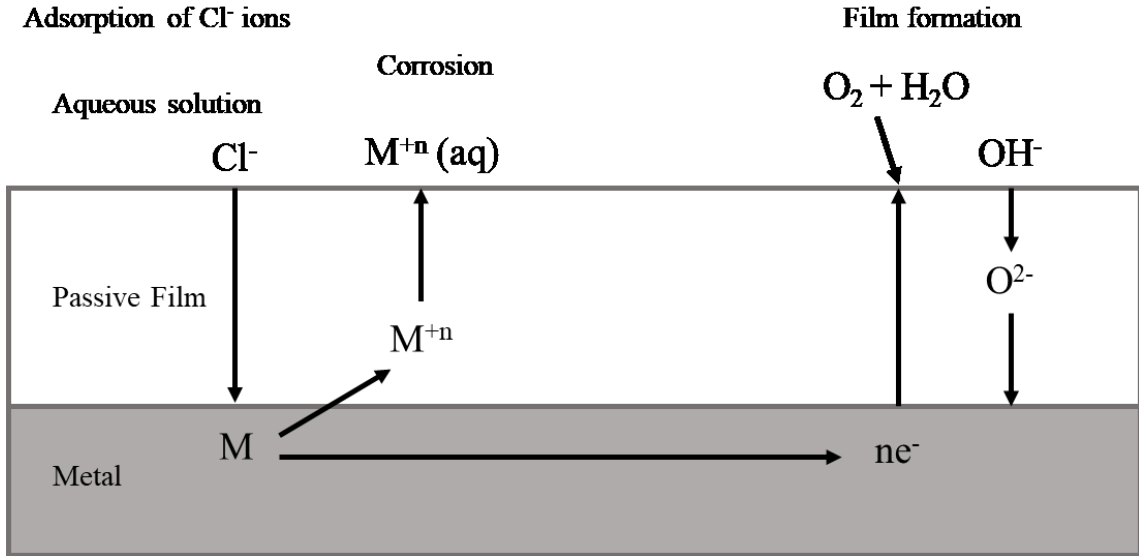
Figure 1-2:   Illustration of the oxide penetration mechanism for the adsorption of chloride ions and its relation to the dissolution of metal ions and reformation of the passive oxide layer [4].

In stainless steels MnS inclusions are thought to have an important role in initiation of pitting corrosion. Manganese is added to stainless steel to prevent the formation of unstable FeS, by instead forming MnS which is more stable. SS316 has approximately 2% manganese added for this purpose [4,11]. The mechanism for inclusion induced corrosion is not fully understood but several theories exist [4,11,14,15].

The most common theory [11,15,16] is that MnS inclusions dissolve, leaving sulfur containing compounds, such as thiosulfate or sulfates, near the inclusion. This acidifies the electrolyte near the inclusion.

$$M_{(aq)}^{n+} + H_2O \rightarrow MOH^{(n-1)+} + H_{(aq)}^+ \qquad (2)$$
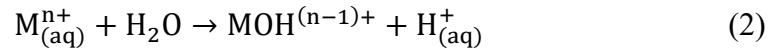
This acidification makes dissolution of the now exposed metal surface more favourable and leads to a stable pit being formed. If the sulfur cap breaks the electrolyte returns to a more neutral pH, corrosion products diffuse away and corrosion in the pit stops [11,16]. This repassivation occurs during periods of "meta-stable pitting". It has also been proposed that MnS inclusions dissolve due to Cr and Fe diffusing into the inclusions during manufacturing. This forms a Cr depleted region around the pit which can lead to dissolution of the metal surrounding the inclusion. This metal dissolution leads to an acidic environment that renders the inclusion unstable, eventually causing it to dissolve [15]. Dissolution of the MnS inclusion leads to a highly acidic environment that can lead to pit formation.

The water treatment is intended to preferentially remove MnS inclusions by dissolution before electrochemical testing, thereby improving corrosion resistance [14]. However, it is important to note that MnS is only slightly soluble in water with a solubility of only 6 mg/L at 20 °C [17]. For this reason, a large quantity (1.5 L) of highly pure water at high temperature (90 °C) is used to maximize dissolution.

Molybdenum (Mo) plays an important role in preventing pitting corrosion in stainless steels, it is the addition of Mo that enhances the corrosion resistance of SS316 compared to SS304 [18]. One proposed mechanism is that charged Mo^{6+} species in the oxide layer interact with cation vacancies (negatively charged) to prevent Cl^- ions from

moving through the oxide layer [4]. A related theory expands on this, to propose that

molybdate anions (i.e., MoO_4^{2-}) migrate to the oxide surface and form a cation selective

layer (negatively charged). This in turn causes the oxide layer closer to the metal surface

to become anion selective (positively charged) creating a bipolar oxide layer. This

prevents the penetration of the oxide layer by Cl⁻ ions as well as increasing the migration

of O^{2-} ions, which in turn improves the rate of oxide formation [4,12,19]. The increased

migration of O^{2-} comes from the breakdown of hydroxide ions in the oxide layer [19].
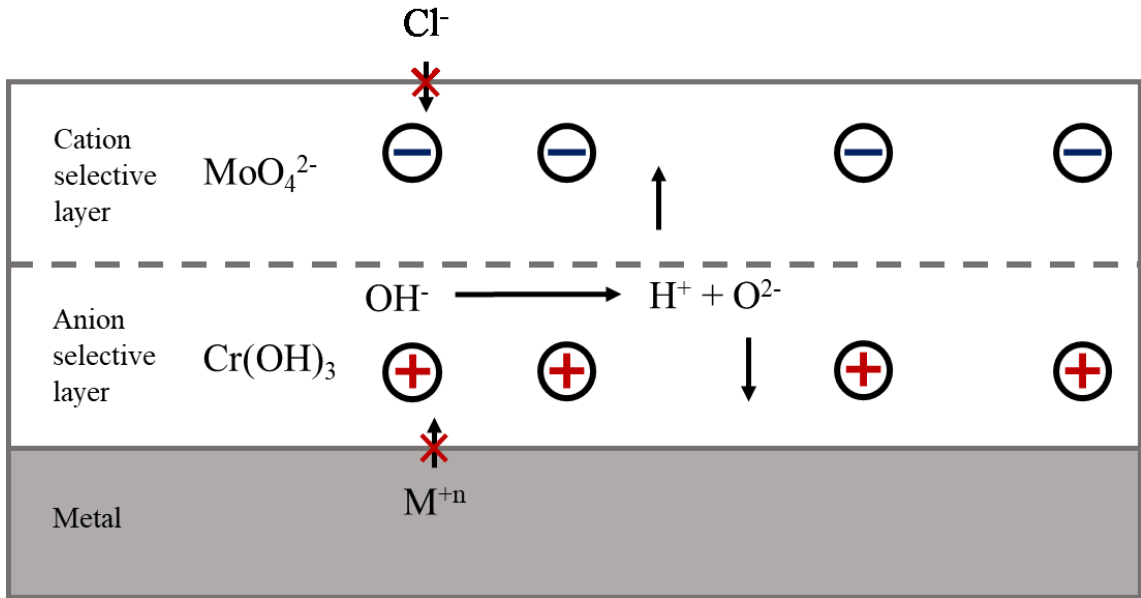
Figure 1-3:   Illustration of the bipolar model for the effect of molybdenum in the
               corrosion resistance of the stainless steel oxide layer [19].

1.5 X-Ray Photoelectron Spectroscopy

XPS is a commonly used surface science technique, which helps to determine the

chemical composition of materials by measuring the energy spectra of electrons

generated by the photoelectric effect. XPS has a high level of surface sensitivity, and only

measures the composition of a material within the first few nm from the surface [20]. This feature makes it ideal for looking at oxide layers on metals or other thin films. The technique uses x-rays of a known energy to excite photoelectrons from the sample's surface. When an x-ray of sufficient energy is absorbed it can excite electrons out of the atom's core energy levels and into the vacuum as shown in Figure 1-4. The emitted electrons lose an amount of energy called the binding energy, E_b, which depends on the element. Emitted electrons then travel to a detector which measures their kinetic energy, E_k, spectrum. There is also a work function, ϕ, associated with the instrument which needs to be accounted for. All these energies are related by the following equation:

$$E_b = h\upsilon - E_k - \Phi \tag{3}$$

where hυ is the incident x-ray's energy and depends on the instrument's source. These energies are further illustrated in Figure 1-5. Electrons are absorbed or scattered very easily so XPS experiments need to be carried out under vacuum to minimize scattering of electrons by gas molecules. However, in addition, XPS is carried out under ultra-high vacuum conditions ($\sim 10^{-9}$ torr) to minimize the adsorption of gases onto the sample surface.
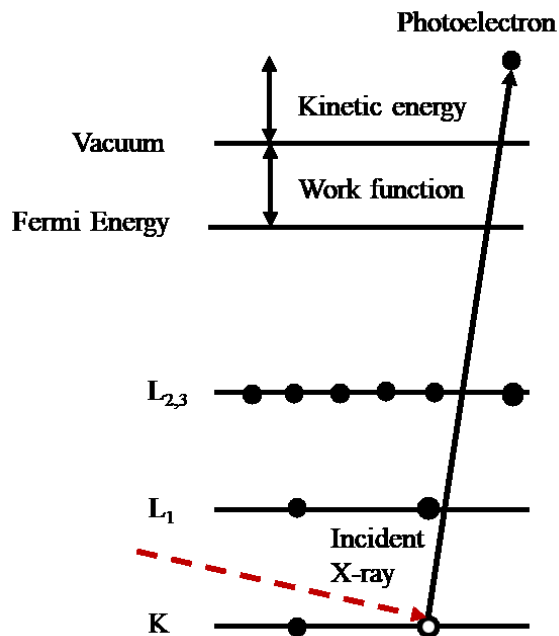
Figure 1-4:   Diagram showing the ejection of a core electron by an incident x-ray. This creates a photoelectron with a kinetic energy characteristic of the chemical species emitting it.
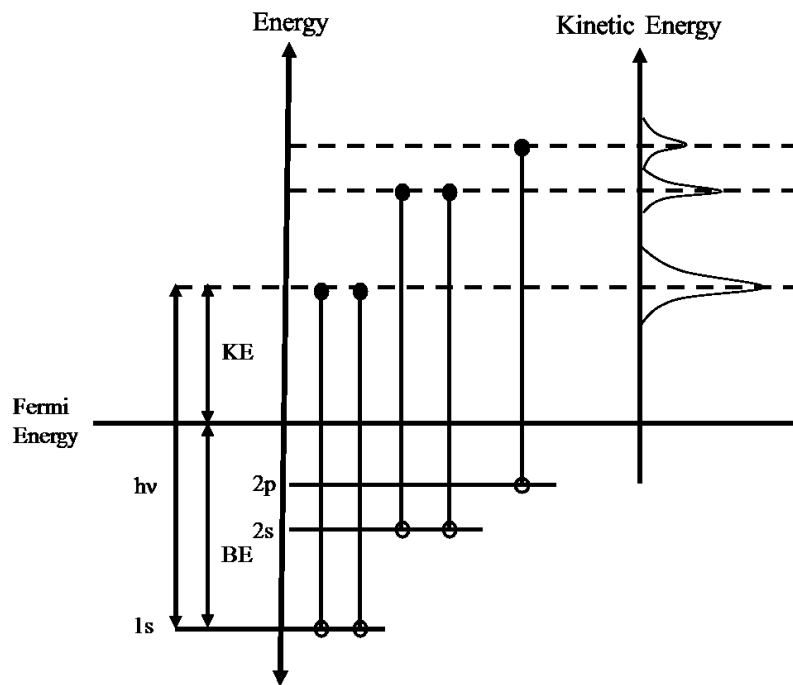
Figure 1-5:   Representation of the energy levels in an atom and their relation to the plotted spectra for kinetic energy (KE), or similarly binding energy (BE).

X-ray generation in XPS is an important area to address when discussing the technique. X-rays are generated using a phenomenon called x-ray fluorescence (Figure 1-6). This is the same process that generates characteristic x-rays in SEM. A high energy stream of electrons is generated from a filament and accelerating potential. The electrons then hit a water-cooled metal target (usually magnesium or aluminum on a copper base) [20,21]. An example of a twin anode x-ray source is shown in Figure 1-7. The incident electron ejects a core electron from the atom, a valence electron then drops down in energy to fill the core vacancy releasing an x-ray in the process. In theory this would generate x-rays of a single, clearly defined energy, but in practice generated x-rays cover a continuous spectrum with a higher energy tail that goes up to, but not above, the accelerating voltage (in Figure 1-8 this cutoff voltage is 15 kV). This phenomenon is shown in Figure 1-8 for Al Kα radiation, this is the same radiation that was used in this work and has a peak energy of 1486.6 eV. This is caused by x-rays interacting with the metal target after generation and loosing energy. Kα refers to the energy levels involved in generation, in this case an electron decaying from the 2p orbital to the 1s orbital. Monochromators can be used to create a narrower energy peak but this reduces the signal leading to longer scan times. Scans can be much faster using synchrotrons, as synchrotron radiation can be more than six orders of magnitude more intense than the radiation from normal x-ray tubes [22]. Modern synchrotrons, like the Canadian Light Source, can use insertion devices called "undulators" and "wigglers" to create even more intense radiation over a narrower range of energies [23].

Monochromators can also lead to sample charging. In a non-monochromated instrument Bremsstrahlung radiation, caused by inelastic scattering of electrons, excites

low energy electrons from the sample holder and aluminum window. These electrons are electrostatically attracted to the positively charged sample preventing charging, albeit with a slightly positive equilibrium potential [20]. The initial charging is caused by photoemission from the sample, which results in a net positive charge. In monochromated instruments, Bremsstrahlung radiation is filtered out which prevents this anti-charging mechanism, instead low energy electrons need to be intentionally added using a purpose-built filament [20]. With conductive metallic samples, like the ones used in this work, charging is not a major issue.

Another small challenge is referencing the XPS spectrum to a known energy. Fortunately all samples tend to have a small amount of adventitious carbon on the surface and carbon monoxide will tend to adsorb onto the sample surface over time. This means there is always a guaranteed peak from carbon in the spectrum. All XPS spectra use the C1s peak as a reference point and set it to be at a binding energy of 284.8 eV.
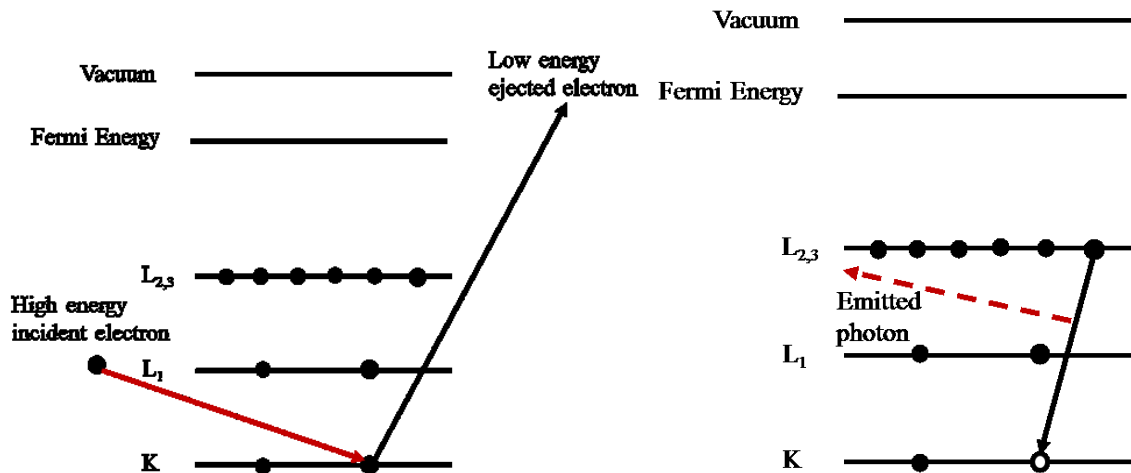
Figure 1-6:   Energy diagram showing x-ray fluorescence. This is a two-step process where a high energy incident electron ejects a core electron. A valence electron then drops down in energy to fill the vacancy, in the process releasing an x-ray of known energy.
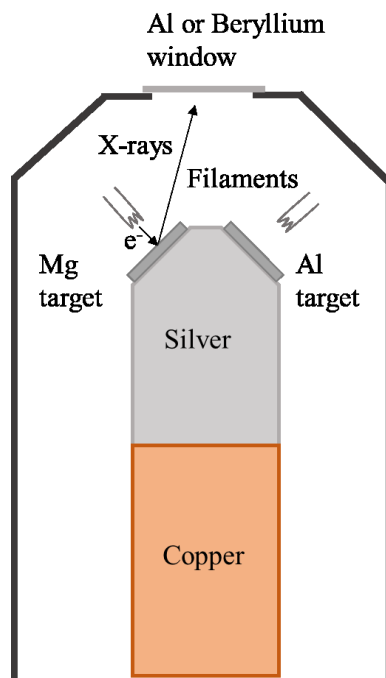
Figure 1-7:   Schematic diagram of a typical twin anode x-ray source for XPS, generally the copper base would have some form of water cooling as well. The silver substrate is used to minimize contamination of the x-rays by Cu Lα radiation as the metal targets degrade [24]. Based on a diagram of a Thermo Scientific XR3 x-ray source [24].
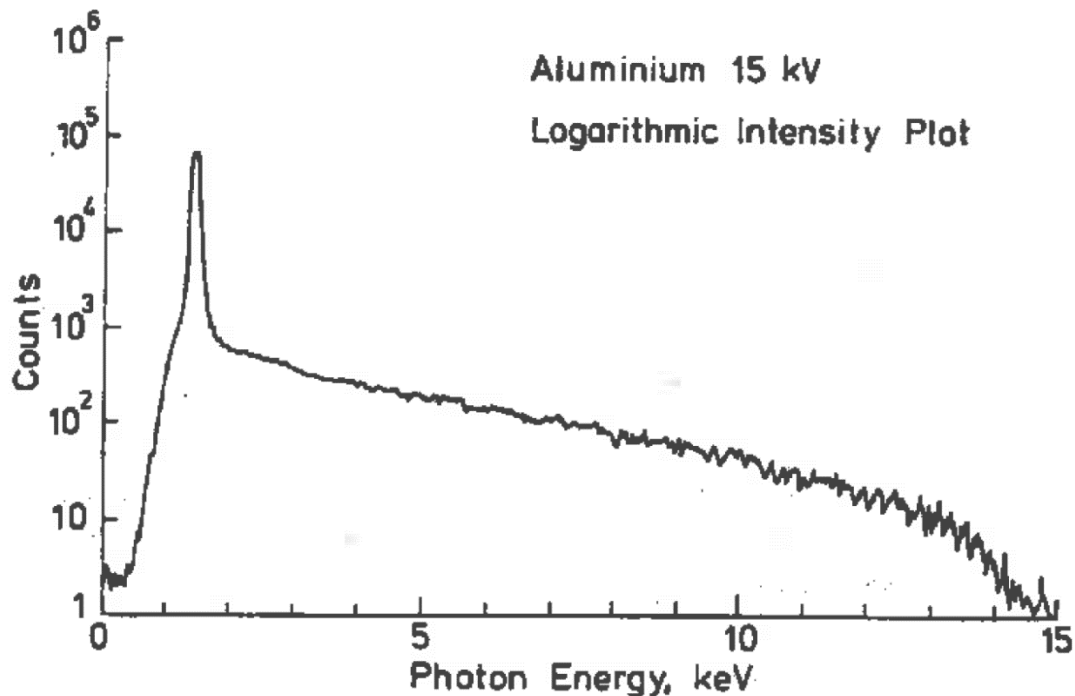
Figure 1-8:   Al Kα x-ray spectrum, generated by bombarding an aluminum target with 15 keV electrons. This is the same experimental setup as the x-ray source used in this work and illustrates the relatively broad nature of this peak. It is worthwhile mentioning that the electron energy can be determined from this graph by looking at the highest energy photons being generated. This spectrum can be narrowed using monochromators. Figure taken from [20].

In addition to photoelectrons, Auger electrons are also generated, and can be detected in XPS spectra. Auger electrons are caused by higher energy valence electrons relaxing into core states. This causes a virtual photon that excites valence electrons from the metal. The first step of this process is very similar to the second step of x-ray fluorescence. These emitted electrons have an energy independent of the x-ray source. This energy independence allows them to be identified easily by changing the x-ray source. Their nomenclature depends on the energy levels involved in the transition, for example a 2s (L_1) electron decaying to a 1s (K) state and exciting a 2p ($L_{2,3}$) electron is called a KLL Auger transition [21]. This type of transition is shown in Figure 1-9. Auger

16

electron production competes with characteristic x-ray generation which is relevant for SEM and will be explained in the next section, and both depend on atomic number. Characteristic x-rays are dominant at higher atomic numbers, with a crossover point at an atomic mass of approximately 33 [21].
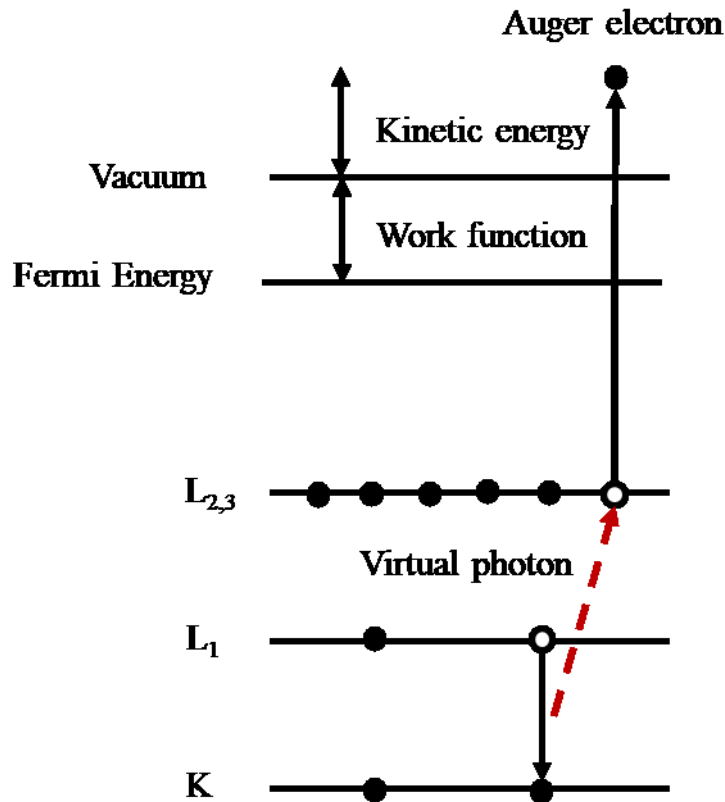
Figure 1-9:   Diagram of the Auger electron emission mechanism. The example shown above is a KLL type emission. In this case an L_1 electron relaxes into a K hole, emitting a virtual photon that ejects an $L_{2,3}$ valence electron.

An important feature to address is spin-orbit splitting. Looking at the example of the $2p_{1/2}$ and the $2p_{3/2}$ peaks, p orbitals have an orbital angular momentum quantum number, l, of 1. Any unpaired electron can either have its spin, s, and orbital angular momentum parallel or antiparallel. Calculating its total angular momentum quantum number [20]

$$j = l + s \tag{4}$$

gives a value of either 3/2 or 1/2. The degeneracy of these two states can be calculated from:

$$degeneracy = 2j + 1 \tag{5}$$

giving 2 electrons in the $2p_{1/2}$ state and 4 electrons in the $2p_{3/2}$ state, this gives an area ratio for the two peaks of 1:2.

An understanding of XPS backgrounds is also important, in general at low binding energies the background is dominated by low energy electrons from Bremsstrahlung radiation. At higher energies the background has a step like nature, increasing on the low kinetic energy side of peaks, this is primarily caused by electrons that have had their kinetic energy reduced by scattering events. Larger steps are generally indicative of the element responsible for the peak being at a greater depth inside the sample. This is qualitatively shown in Figure 1-10 [20].
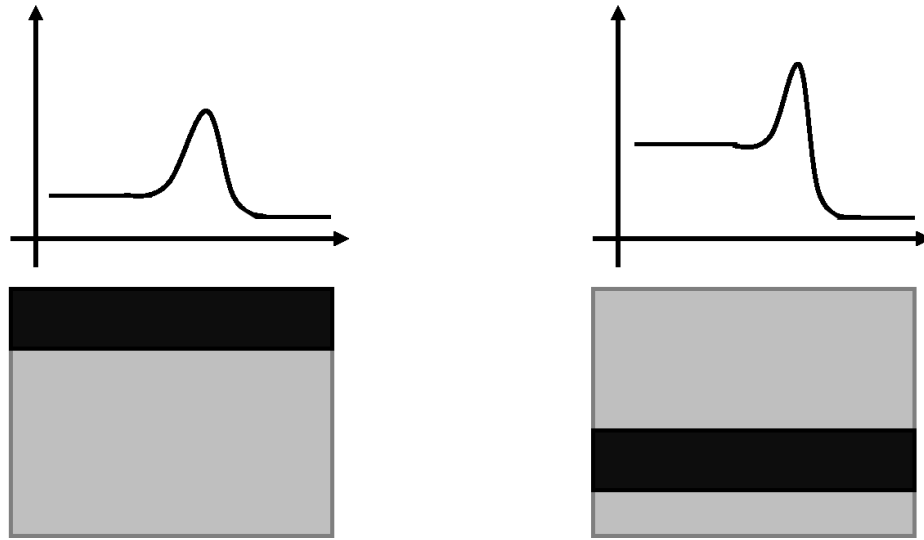
Figure 1-10:   Qualitative representation of the effect element depth has on an XPS
background, with elements further from the surface contributing more to
the background.

Generally, XPS peaks are approximately symmetric and can be fitted using a

hybrid of Gaussian and Lorentzian peaks. Metals are an exception and tend to have

asymmetric peaks. This asymmetry is caused by empty states near the Fermi energy.

During photoemission valence electrons can be excited to these empty states. The energy

that they gain by moving to the empty higher energy state is then unavailable to the

photoelectron. This causes a low kinetic energy tail on the metal's spectrum. A higher

density of states at the Fermi energy will lead to greater peak asymmetry [20].

As mentioned earlier, XPS is a surface sensitive technique, which only gains

information from electrons generated in the first several nm of material. This is because

as photoelectrons travel out of the material to the detector they scatter off atoms in the

lattice, and scattered electrons will not contribute to defined peaks, instead contributing to

the background. The vast majority of the signal (~95%) is generated by the top 4-10 nm

of the sample for perpendicular departure of the electrons [20].

1.6 Scanning Electron Microscopy

The pits and surface features being investigated in this research are often on the order of a few μm. Conventional optical microscopes are limited in their effectiveness by the diffraction limit

$$d = \frac{\lambda}{2n \sin \theta} \tag{6}$$

where d is the resolution, λ is the wavelength of the light and $n\sin\theta$ is a quantity known as the numerical aperture (usually slightly greater than 1). A good first approximation is that this diffraction limit is equal to $\lambda/2$. For visible light this gives a resolution of approximately 250 nm. This is a best case scenario for a high quality microscope and would still result in relatively blurry images. In order to get to higher resolutions the easiest way is to use shorter wavelengths such as UV, X-rays or electrons. SEMs can use electrons between 500 eV-50 keV, but typical SEMs have electron beam energies between 20 keV-30 keV [21]. As an example, 10 keV electrons have a de Broglie wavelength on the order of 1 Å, approximately 10,000 times smaller than visible light. It is important to clarify that SEMs do not have 1 Å resolution, because the limiting factor is the spot size of the electron beam. Which is primarily affected by electron energy and the quality of the electromagnetic lenses, this still gives typical resolution on the order of 10 nm which is still much better than optical microscopes [21].

Another significant difference between SEM and optical microscopy is that SEM does not involve electrons passing through the sample, there is a distinct technique called transmission electron microscopy (TEM) which requires much thinner samples but offers

better resolution. Many optical microscopy techniques involve transmission through the samples, which can be problematic for opaque, non-reflective samples.

An SEM consists of an electron source, often a tungsten filament, several electromagnetic lenses, apertures, deflector coils and a detector as shown in Figure 1-11. The focussed electron beam is then rastered across the sample surface in much the same way as an atomic force microscope probe is scanned across a surface. Unlike light, electrons strongly interact with air, therefore SEMs generally require good vacuum conditions to maintain high quality images, however environmental SEMs can operate at much higher pressures allowing for wet samples. In general though, vacuum conditions make imaging wet samples difficult. It also means that as the sample is bombarded by electrons it will become charged, charged sections will then repel incident electrons leading to image artifacts. For this reason, SEM works best with metallic or highly conductive samples. When imaging biological samples gold or carbon is often sputtered onto the surface to improve conductivity.

Electron source

Aperture

Condenser lens

Aperture

Condenser lens

Deflectors

Detector

Condenser lens

Aperture

Sample
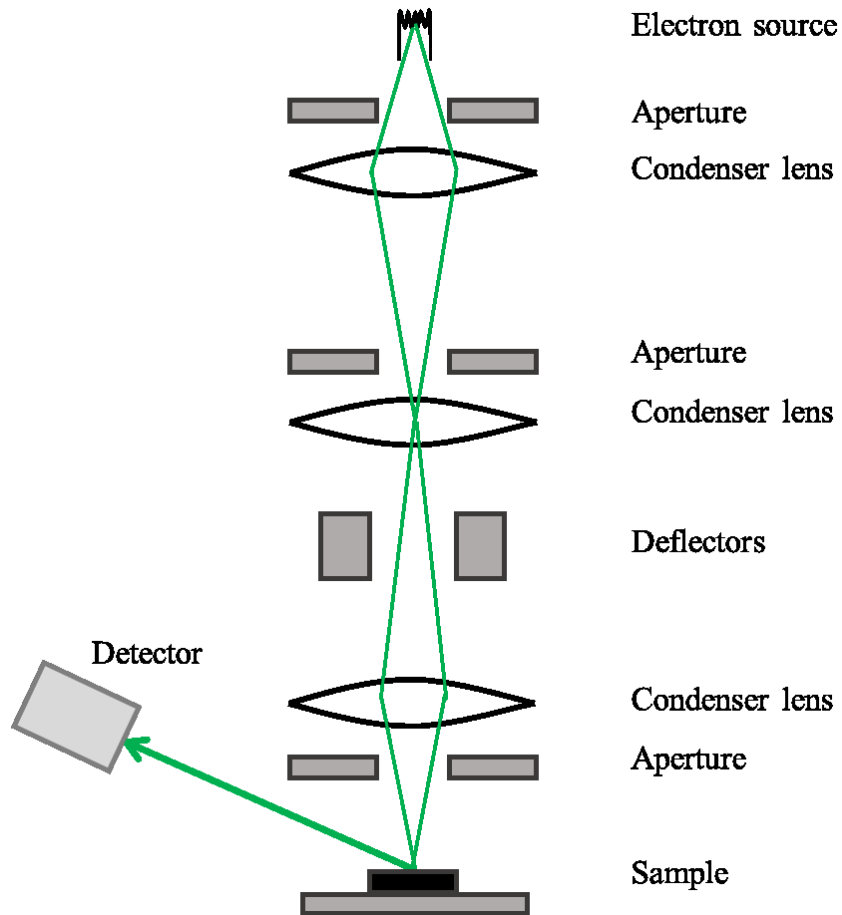
Figure 1-11:   Schematic of an SEM showing the similarities with optical microscope [21]. Instead of using glass lenses they use electromagnetic lenses, the entire system also needs to be under vacuum to prevent electron scattering.

Incident electrons interact with matter in several different ways. These processes are characteristic of different depths, for example Auger electrons are low energy so they are only observed at very shallow depths due to electrons having a short mean free path at low energies. As mentioned earlier, Auger electrons are generated when incident electrons eject a core electron from an atom, a valence electron then fills the core vacancy creating a photon which ejects another valence electron as depicted in Figure 1-9. This final ejected electron is referred to as the Auger electron [21]. X-rays on the other hand

can penetrate a much greater thickness of material, this means that characteristic x-rays are measured from a much greater volume of material, giving less resolution.

Backscattered electrons are electrons from the original electron beam that have been reflected back along their original path by elastic scattering. These electrons usually retain a large amount of their initial energy, and are defined as having energies greater than approximately 50 eV [21]. Auger electrons are also considered to be backscattered electrons, despite the processes being different [21]. Backscattered electrons are useful because they generate contrast between different atomic weights [21].

Secondary electrons, which are the main electrons used in SEM imaging, are generated when incident (i.e., primary, or backscattered) electrons are inelastically scattered by an atom's valence electron. These electrons are defined as having energy less than approximately 50 eV [21]. Secondary electrons are further subdivided into SEI, SEII and SEIII. SEIs are created from primary electrons interacting with the sample, SEIIs are created from backscattered electrons interacting with the sample and SEIIIs are from backscattered electrons interacting with material outside of the sample. SEIIs and SEIIIs are undesirable and reduce image resolution because they originate from areas unrelated to the area the beam is scanning [21].

The final interaction is the generation of characteristic x-rays which are created when valence electrons fill core vacancies emitting x-rays. These x-rays are characteristic of specific elements and can be used to identify the chemical makeup of samples, a technique called energy dispersive x-ray spectroscopy (EDS). Characteristic x-rays are closely related to Auger electron emission and occur as competing processes. As mentioned earlier Auger electron emission is the dominant process at lower atomic

numbers, where the electrons are less tightly bound, whereas characteristic x-ray emission occurs more often at higher atomic numbers [21].

1.7 Ellipsometry

Ellipsometry is an optical technique where light of a known polarization is incident on a planar sample. The reflected light's polarization is measured, and the change can be used to determine properties of the sample surface [25]. If the composition of a thin film, such as an oxide layer, is known software can be used to create a model allowing the determination of the oxide layer thickness. Ellipsometry is a non-destructive and rapid technique for measuring oxide thickness on metal samples.

Samples measured by ellipsometry require high reflectivity, and the oxide layer should not be too thick (film thickness should be on the order of $\lambda/2$ or less, where λ is the wavelength of the incident light [25]).

CHAPTER 2: METHODS

2.1 Sample Preparation

Samples were made from 5 mm side length, square plates of 0.9 mm thick SS316. Samples were cut to size in the machine shop and attached to metal "pucks" using Crystalbond™ melted using a heat gun. Four samples were attached to each puck to give a larger effective footprint to make maintaining a flat base easier. They were then polished sequentially using silicon carbide (SiC) sandpaper pads (320 and 600 grit) lubricated with tap water at 150-210 rpm. This step was followed by diamond suspensions on cloth pads (9 μm, 1 μm) lubricated with nanopure water (resistivity of 18.2 MΩ·cm indicating extremely high purity, made from distilled water after multiple filtration processes [26]; Barnstead™ Nanopure™ system) at 110 rpm. Polishing was done on a Buehler Beta Grinder Polisher, other polishing supplies (i.e., SiC sandpaper pads and diamond suspensions) were also bought from Buehler. Samples were held in one direction for approximately two minutes before being rotated 90º and polished until all previous polishing lines were removed.

Earlier experiments using this polishing technique had more intermediate steps, but these were discarded as they were found to be redundant. The quality of polishing was checked using a low-magnification binocular microscope. After polishing, samples were removed from the Crystalbond™ by sonication in acetone, and then rinsed using acetone, followed by ethanol and deionized water. Prior to testing samples were stored in petri dishes polished face up on Kimwipes™.

Before electrochemical testing polished samples had to have electrical contacts attached to their unpolished face. In this work copper wires were soldered to single-sided copper SEM tape, which was then attached to the unpolished side of the sample using the tape's adhesive. Heat treated and electropolished samples had such thick and insulating oxide layers that this method did not give a sufficiently good electrical contact, so the technique was modified and the back of the samples were sanded using 600 grit SiC pads to expose a fresh surface. During this sanding samples were placed face down on the finger of a nitrile glove. Excessive heating of the SEM tape adhesive during soldering also tended to cause bad electrical contacts. To test for a bad electrical contacts, the resistance of the electrical contact was measured using a multimeter. Samples typically had less than 1 kΩ total resistance.

Finally, any exposed metal was covered with lacquer (nail polish) to prevent the electrolyte coming into contact with unprotected copper or the unpolished edges of the stainless steel samples. Copper would corrode before the sample, and the unprotected sample edges tend to corrode at lower potentials due to crevice corrosion and a more damaged surface [4]. Enough lacquer was used to fully cover the sample's back and sides, but leave as much surface uncovered as possible, this was to maximize the sample size to improve the chances of pitting corrosion. This large sample size did create the problem that the optical microscope beam did not fully cover the sample, meaning that often corrosion would occur off-camera. Also because of the irregular nature of painting around the edge of the surface, sample surface areas were not kept constant, and therefore were not recorded. For this reason, currents in the current-voltage scans shown later are presented simply as currents instead of current densities.

Prior to testing on SS316 plates, similar measurements were done ont SS316 wire

samples. The polishing procedures and testing were almost identical. These

electrochemical trials will not be presented in this thesis because the reference electrode

used at the time was much less reliable than the current one. Techniques used to

minimize the instances of crevice corrosion also did not work as well as those used for

SS316 plates. However, it is worth mentioning these trials, as SEM images of corroded

wire samples will be presented in this work. Due to the samples being wires, they could

be attached to the testing apparatus directly. Wire samples were protected from crevice

corrosion using heat shrink tubing and epoxy to give a very tight fit around the polished

surface. Unfortunately, this method still tended to allow some crevice corrosion around

the sample edges if there were any gaps or bubbles in the epoxy. Finally, due to their

smaller surface area, the probability of having impurities or imperfections in the surface

to serve as corrosion initiation sites is lower for wire samples. Smaller sample surface

areas lead to a higher critical pitting potential.

2.2 Surface Treatments

In this work four different surface treatments were used, as well as an untreated

control to determine which were most effective at improving the corrosion resistance of

SS316. The first two treatments tested involved heating the samples in deionized water

and dilute hydrogen peroxide. These are useful because they are similar to actual

disinfection techniques used in hospitals for stainless steel instruments such as steam

sterilization [27]. Electropolishing was also used, which is the industry standard for

polishing many stainless steel products such as water bottles and tools [28,29]. Finally, samples were heated in an oven to see if a thicker oxide layer led to better corrosion resistance.

2.2.1 Untreated

The first samples tested were given no additional treatment, other than polishing, to give a baseline performance for SS316. These samples acted as a control.

2.2.2 Water Treatment

A proposed method to remove manganese sulfide (MnS) inclusions is to heat the sample in nanopure water preferentially dissolving the MnS inclusions [14]. In this process samples were placed in 500 ml of 90 ˚C nanopure water for 3 hours with the water being changed every hour. The water was contained in a Teflon™ container, shown in Figure 2-1. Temperature was maintained using a Haake F3 water bath. Before water changes, the water was preheated in a clean glass beaker using a hotplate to make the treatment as close to continuous as possible. Samples were held in a Teflon™ holder in the container to make removal after treatment easier. One challenge is that the holder, which was a bar of Teflon™ with perpendicular cuts used to hold the samples like a toast rack, prevented the water from touching one corner of the sample. To minimize this, as little of the sample was held in the holder as possible, and the untreated corner was coated in lacquer.

Figure 2-1:   Photograph of the Teflon™ container and sample holder used in the water treatment as well as in the hydrogen peroxide treatment.

2.2.3 Hydrogen Peroxide Treatment

Hydrogen peroxide is an unstable chemical, that when heated breaks down to water and releases oxygen in the process. This process also occurs at room temperature, but at a much slower rate.

$$2H_2O_2 \xrightarrow{\Delta} 2H_2O + O_2 \tag{7}$$

This oxygen can theoretically be used to thicken the oxide layer of metals heated in an oxidizing solution of hydrogen peroxide [30]. In this work, stainless steel samples were heated in 500 mL of a 3% solution of hydrogen peroxide (Sigma Aldrich) in nanopure water at 90 ˚C for 2.5 hours. The solution was held in a Teflon™ container, Figure 2-1, while temperature was maintained using a Haake F3 water bath. The solution was not

changed during the treatment. The same issue where one corner remained untreated occurred for the hydrogen peroxide treatment.

2.2.4 Electropolishing

A commonly used technique for polishing stainless steel products is electropolishing. Objects are immersed in acidic solutions while a positive voltage is applied to the sample causing the removal of surface material. Due to the enhancement of electrical fields near sharp points the process preferentially removes discontinuities from the surface leading to a smooth surface finish. A major advantage of electropolishing is that it allows rapid and cost-effective polishing of geometrically complex objects. The largest drawback is that it uses very strong acids which are relatively expensive and can be environmentally damaging through chemical waste. In this work the solution used was 60% (by volume) phosphoric acid, 20% sulfuric acid, 10% glycerol (which served as a thickening agent) and 10% deionised water [8]. The solution was heated to 65-70 ˚C and a potential difference of 5 V was applied for 3 minutes. The solution was stirred using a Teflon™ coated stir rod. Other methods suggest aerating the solution [31].

The process was done in a 50 mL beaker to minimize chemical waste. Samples were held in the upper corner with copper alligator clips to minimize the unpolished area. A counter electrode made from bent copper wire, with a surface area greater than the working electrode was used. Electrode separation was approximately 3 cm and the solution was stirred using a Teflon™ coated stir rod during the polishing procedure. Before electropolishing, samples were only ground with 600 grit SiC pads, instead of being polished to a mirror finish.

Figure 2-2 shows an approximate current voltage graph for a metal in an acidic electropolishing solution. Direct measurements were attempted to determine the flat polishing regime for SS316. Unfortunately they were not conclusive and instead showed a relatively continuous linear increase. Similar measurements were done for aluminum and did clearly illustrate the desired behaviour and are presented in Figure 2-3. To determine the ideal polishing parameters for stainless steel, a series of samples were polished at varying potentials for 3 min each. The surface finishes were then qualitatively evaluated for smoothness using an optical microscope.
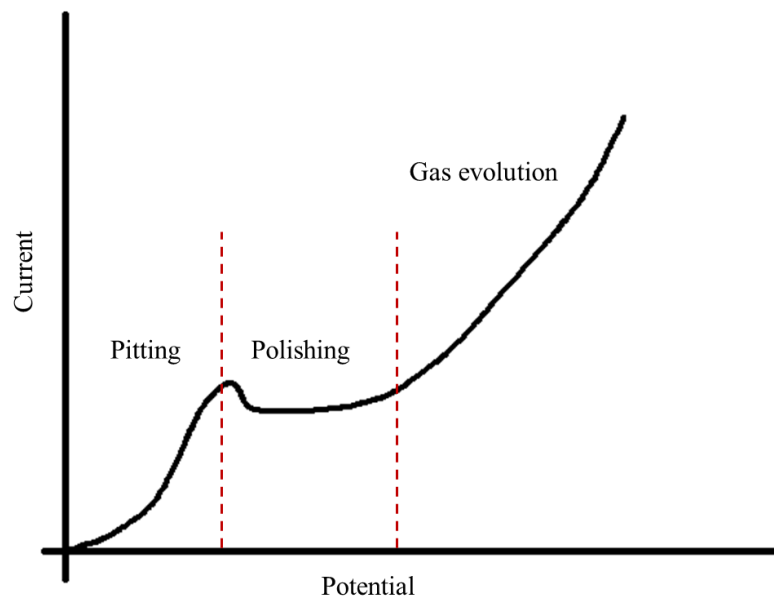
Figure 2-2:   Current voltage graph for electropolishing. Electropolishing takes place in the region where current remains relatively constant as the potential increases. For SS316, this region was found to be in the range of approximately 4-6 V [32].
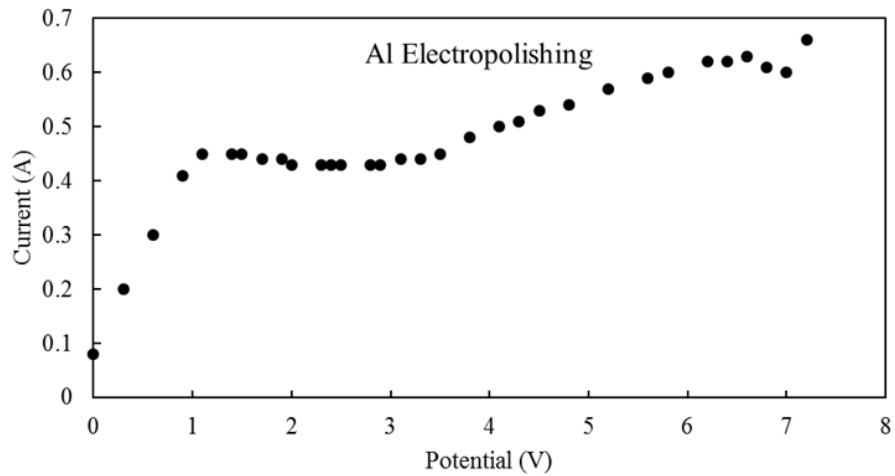
Figure 2-3:   Current voltage graph for aluminum showing an electropolishing region between 2-3 V.

2.2.5 Heat Treatment

Simple heat treatment was also tested as a possible way of increasing the stainless steel's oxide layer thickness. Samples were heated in an oven with a normal atmosphere for 1 hour at 500 ˚C. This treatment gave the samples a reddish-coppery color suggesting a significant change in the oxide layer thickness. Figure 2-4 illustrates this difference in colour.
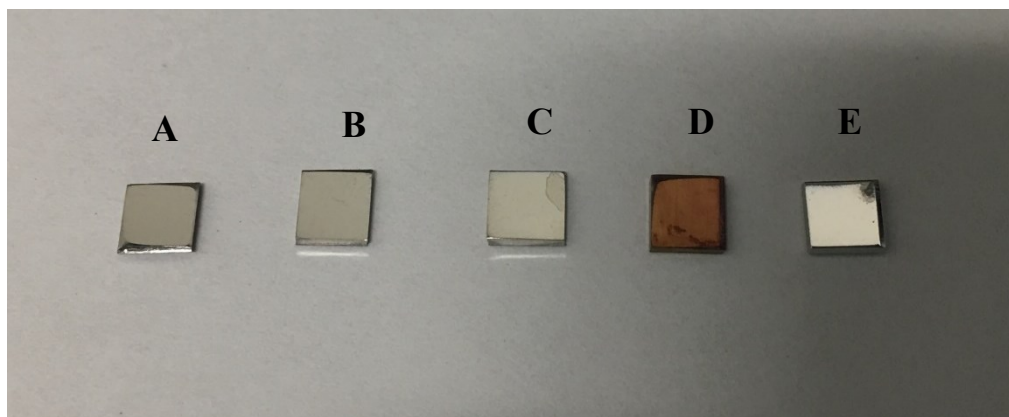
Figure 2-4:   From left to right (A) untreated, (B) water treated, (C) hydrogen peroxide treated, (D) heat treated and (E) electropolished samples. Each sample side length is approximately 5 mm for scale.

2.3 Electrochemical Testing

Samples were tested using a 3-electrode setup, with a platinum counter electrode and a silver/silver chloride in a saturated aqueous KCl solution (Ag/AgCl in saturated KCl, 0.197 V vs Standard Hydrogen Electrode (SHE) [33]) reference electrode. The 3-electrode setup is shown schematically in Figure 2-5. The electrolyte used was a 0.9% by mass solution of sodium chloride (NaCl; ACP) in deionized water. All trials were done at room temperature and standard atmospheric pressure with no deoxygenation (i.e., removing oxygen with argon).

Samples were held in a trapezoidal cuvette, approximately 40 mm wide, 25 mm deep and 30 mm tall. The cuvette was built using microscope slides glued together using AA 349™ Loctite UV-curable adhesive. During construction the glass pieces were supported using an aluminum form. Holes were drilled in the top of the cuvette using a rotary tool with a diamond bit. Tubes, made from glass pipettes, were added on top of the cuvette to help minimize electrolyte evaporation and to stabilize the electrodes. The

central hole was larger and rectangular to accommodate plate samples. Its tower was made using small rectangular pieces of glass. Prior to gluing, the edges of all pieces were ground with 600 grit SiC sandpaper to give a tight seal after gluing.

The glass glue was cured using sunlight over several days prior to testing. After every electrochemical test, the cuvette was rinsed using nanopure water to remove corrosion products. The cuvette was also periodically washed more extensively using sonication and boiling to remove any built-up corrosion products, but this was not done after every trial. The cuvette was connected to a potentiostat using a shielded cable. The cable was connected to the electrodes using a custom-made aluminum holder shown in Figure 2-5. The working electrode was rigidly held in place using a brass screw to make aligning optical microscope images easier.
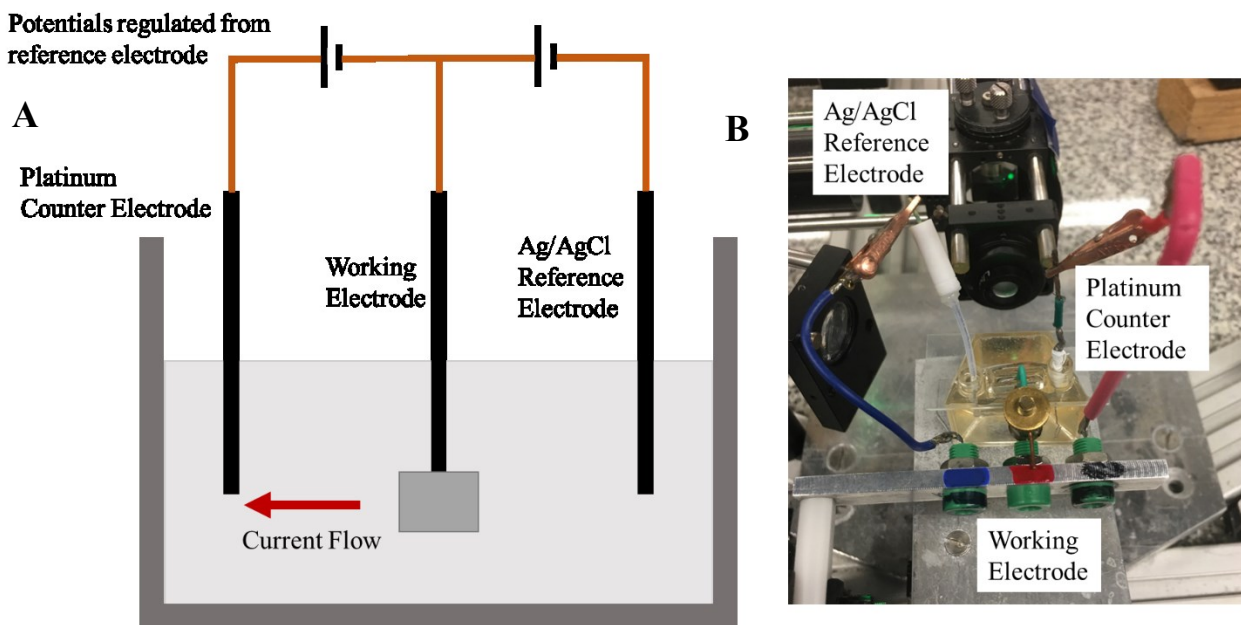
Figure 2-5:   (A) Schematic of a three-electrode electrochemical cell. (B) Picture of the three-electrode electrochemical cell used in this work.

All electrochemical tests were controlled using a Metrohm Autolab B.V. Potentiostat, run using NOVA 2.0 software. Prior to the test starting the open circuit potential (OCP) was monitored for up to half an hour to determine stability, once the OCP was determined to be stable (fluctuating by less than 5 mV) the test would begin. Typically OCPs were between -100 mV and 0 mV. The testing protocol first measured the OCP of the electrochemical cell. The voltage was then slowly increased at a rate of 1 mV/s starting 100 mV below the OCP, up to a maximum of 1.5 V at which point water splitting became a dominant source of current. If a current greater than 0.2 mA (an arbitrarily chosen value) was measured before the voltage reached 1.5 V the program switched the scan direction prematurely, this was to avoid excessively damaging the samples. After changing direction, voltage was reduced to 100 mV below the OCP before ramping to its final value 100 mV above OCP, maintaining the 1 mV/s rate of change throughout. Using this technique, each trial usually took about 1 hour to complete. The trial was then over, and samples were removed from the cuvette, rinsed with deionized water, detached from the copper backing tape, and stored in a plastic bag. If SEM images were taken, samples were sonicated in acetone to remove any nail polish.

A significant challenge encountered during the testing was that many of the hydrogen peroxide treated samples did not corrode during the trials. To account for this, samples that did not corrode were tested a second time. If they again failed to corrode, they were recorded as having a critical pitting potential of 1.5 V, which is the highest value we could test in this experiment using an aqueous solution due to water splitting, as mentioned before.

2.4 Optical Microscopy

While samples were being electrochemically tested, an optical microscope was used to image the sample surface *in situ*. This setup is shown in Figure 2-6. Images of the samples were recorded throughout the electrochemical tests. Samples were illuminated using a 5 mW green LED, and imaged using a Sony XC-ST50 monochromatic CCD camera. The camera has 768 x 494 effective pixels. Images were displayed on television screens and recorded using DVDs. Focussing was done before the test by moving the sample holder and manually adjusting a focussing lens. Fine tuning could be done using a pneumatic 3-axis stage manipulator. Brightness and contrast of the images were adjusted using the television's controls.
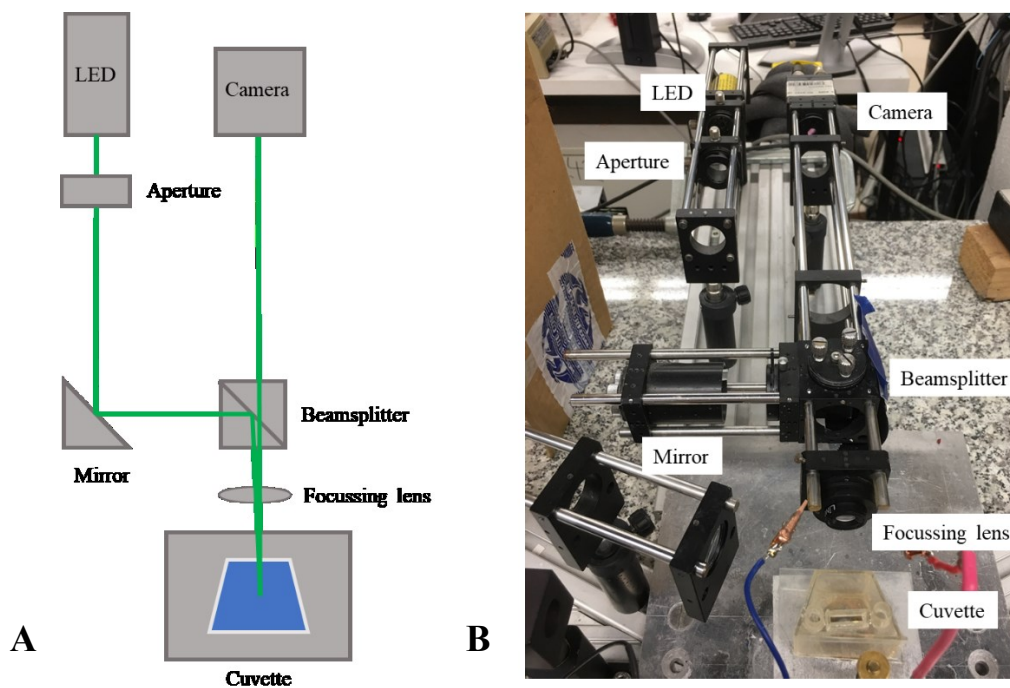
Figure 2-6:   (A) Schematic of the optical microscope setup (B) Image of the optical microscope in the lab.

2.5 Scanning Electron Microscopy

Certain samples were imaged, post-electrochemical testing, both in a top-down and in cross section. A Phenom G2 Pro SEM was used, with samples being attached to aluminum sample holders using either carbon pads or copper double sided tape. Cross sections were made by grinding the samples in a custom-made polishing pucks (Figure 2-7). Samples were secured using mechanical pressure for plates, or Crystalbond™ for wire samples. They were then ground until the desired pit or area of interest was visible in the cross section, as determined by a low magnification binocular microscope. This process was destructive so samples were imaged in the top-down view first to determine areas of interest, before cross sectioning. Before polishing, any nail polish was removed by sonication in acetone. Cross section samples were polished to a mirror finish using the same process as for new samples.
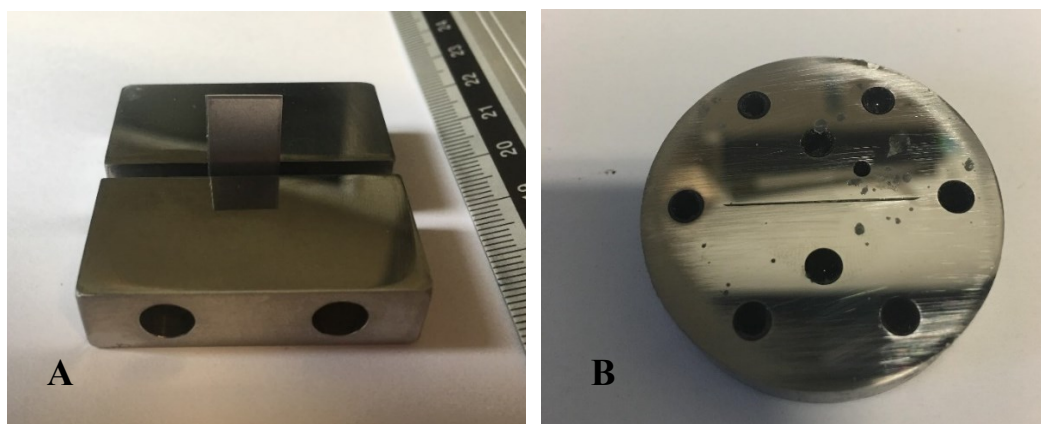
Figure 2-7:   Custom made stainless steel polishing pucks, used to polish cross sections for SEM. (A) Puck for polishing cross sections of SS316 plates. Samples are placed in the middle and secured by tightening the two bolts on the front. (B) Puck for polishing cross sections of SS316 wires, wires are secured in the central groove.

2.6 X-Ray Photoelectron Spectroscopy

Chemical composition of the oxide layer was determined using XPS. Samples that had not been electrochemically tested were measured in an XPS instrument with a ThermoScientific Multilab 2000 spectrometer by A. George. All tests were done using the Al Kα source, operating at 15 kV and 15 mA electron current. The resulting spectra were fitted using CasaXPS software, using Shirley backgrounds. Appropriate constraints were placed on position and line shape using experimental data and online resources [34,35]. The O1s and Cr2p peaks were fitted for all samples.

CHAPTER 3: RESULTS AND DISCUSSION

3.1 Electrochemical Testing

Table 3-1 shows a summary of electrochemical testing results for the different stainless steel surface treatments. As a reminder these potentials are presented relative to an Ag/AgCl in saturated KCl reference electrode which has a potential of 0.197 V when measured relative to a SHE [36]. Electropolished and hydrogen peroxide treated samples exhibited the greatest critical pitting potential which shows that they had the greatest resistance to corrosion. Water treated samples performed moderately better than untreated, but the difference is still significant. Heat treated samples showed the worst corrosion performance of all samples and were the only ones to have a significantly different open circuit potential. Comparing these results to previous measurements on SS316 undertaken by Peter Klages [14], the untreated samples show good agreement. The current work showed an improvement in the critical pitting potential of about 140 mV. This higher resistance to corrosion is probably caused by changes in instrumentation, lower vulnerability to crevice corrosion when using plates and finally a significantly larger number of samples being measured. Water treated results were also consistent with Peter Klages' work [14]. Uncertainties were calculated using a standard error formula and a 90% confidence interval. These results are shown in full detail in Figure 3-1-Figure 3-5. One feature particularly obvious in Figure 3-4 is a large amount of periodic noise; this was only observed during testing in December 2017. The cause is unknown and the oscillations were very low frequency with each cycle taking several

seconds to occur. This effect was also observed in one electropolished trial but none of the other surface treatments exhibited this effect. Tests conducted after December 2017 no longer showed this effect.

Table 3-1: Summary of electrochemical testing results, showing the critical pitting potential where stable pitting begins, and the open circuit potential. Uncertainties were calculated using a 90% confidence interval standard error.

	Critical Pitting Potential, V_{pit} (mV)	Open Circuit Potential, V_{OCP} (mV)	Number of Trials
Untreated	640±70	-70±50	19
Water Treated	770±50	-50±30	19
Hydrogen Peroxide Treated	1390±40	-40±30	28
Heat Treated	200±100	-200±40	8
Electropolished	1050±80	-90±40	15
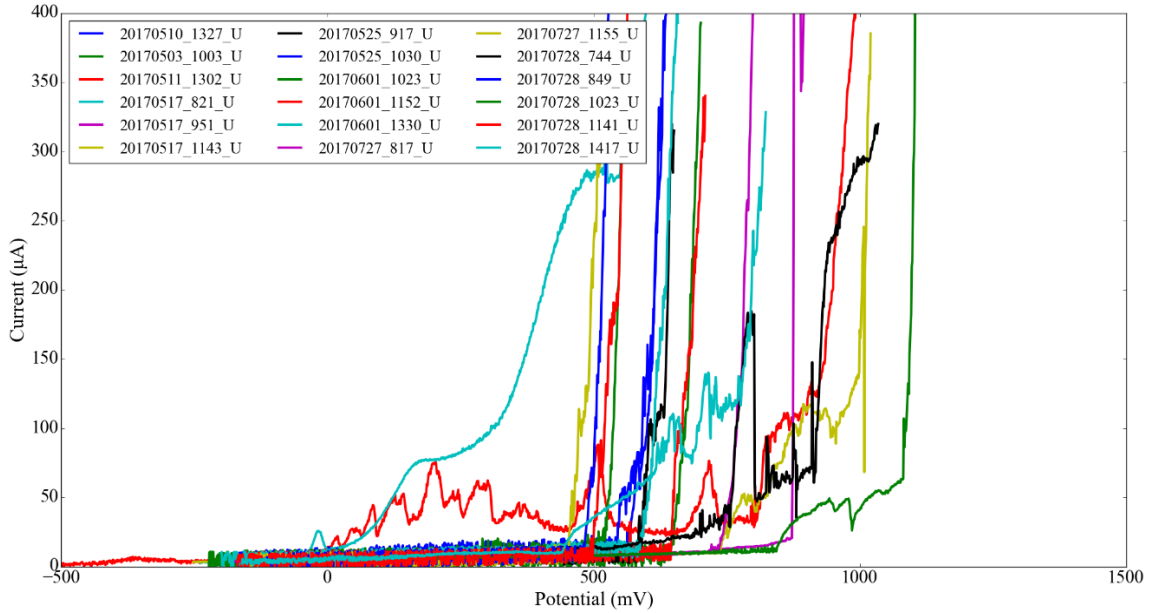
Figure 3-1:   Electrochemical testing results for untreated stainless steel samples. Descent phase of testing is excluded to make the graphs easier to read. Average critical pitting potential was 640±70 mV with a total of 19 samples.
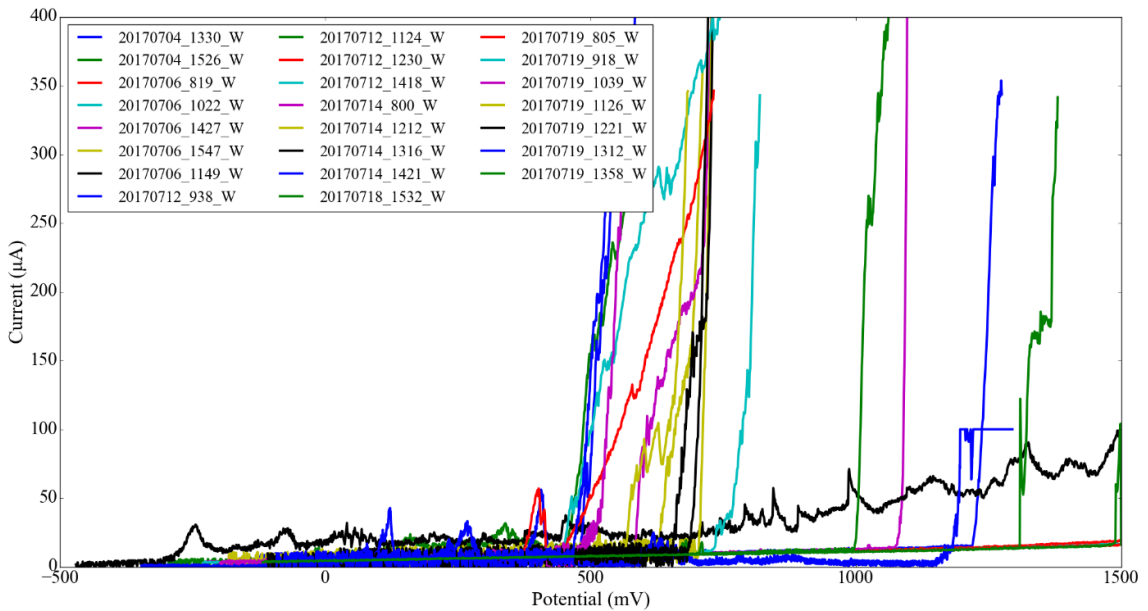
Figure 3-2:   Electrochemical testing results for water treated stainless steel samples. Descent phase of testing is excluded to make the graphs easier to read. Average critical pitting potential was 770±50 mV with a total of 19 samples.

41
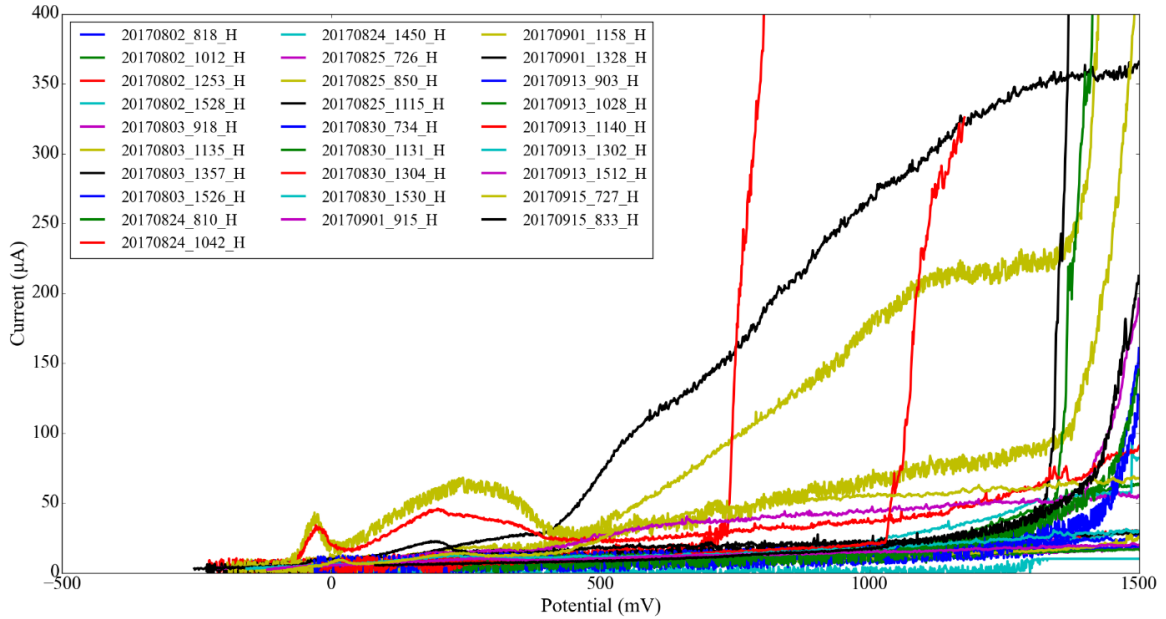
Figure 3-3:   Electrochemical testing results for hydrogen peroxide treated stainless steel samples. Descent phase of testing is excluded to make the graphs easier to read. Average critical pitting potential was 1390±40 mV with a total of 28 samples.
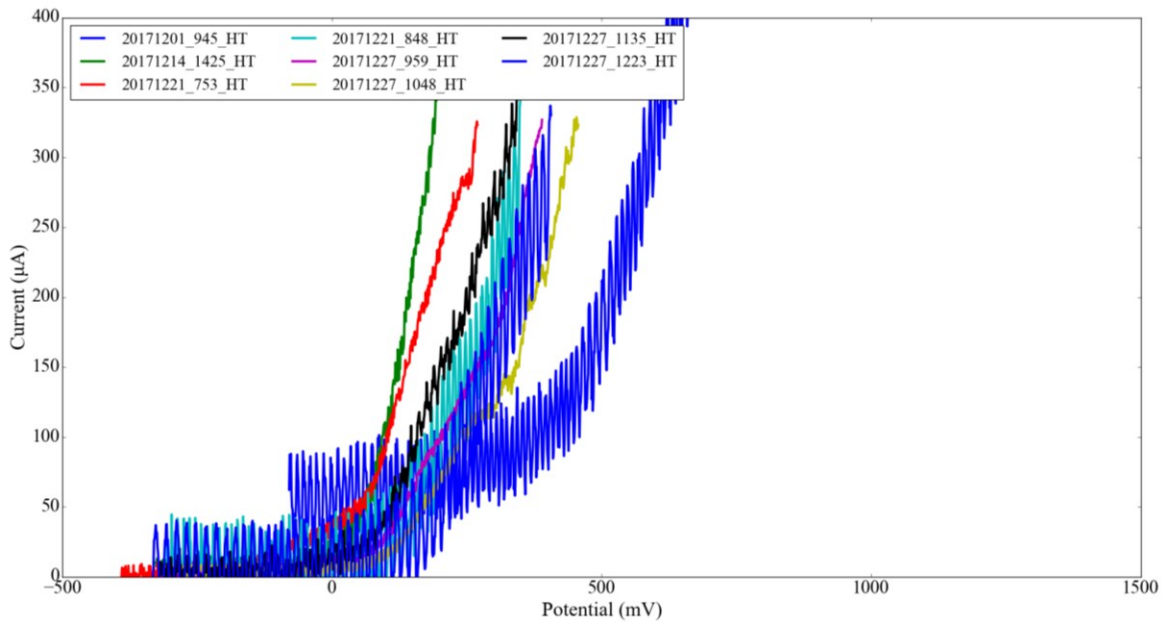
Figure 3-4:   Electrochemical testing results for heat treated stainless steel samples. Descent phase of testing is excluded to make the graphs easier to read. Average critical pitting potential was 200±100 mV with a total of 8 samples.
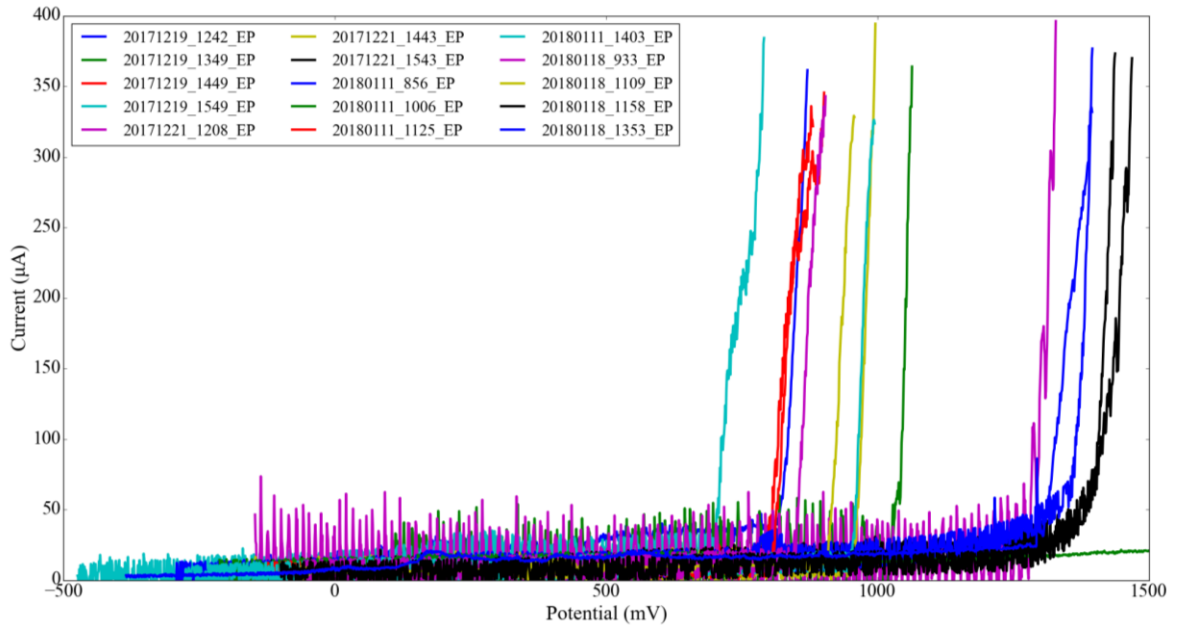
Figure 3-5:   Electrochemical testing results for electropolished stainless steel samples. Descent phase of testing is excluded to make the graphs easier to read. Average critical pitting potential was 1050±80 mV with a total of 15 samples.

During electrochemical testing optical microscopy was recorded simultaneously. Due to the imaged area being smaller than the total sample surface generally corrosion occurred off screen. Figure 3-6 shows a rare case where individual corrosion events can be directly correlated to spikes in the current time graph. Corrosion pits appear as black areas on the surface, with polished metal showing up as grey. The black curve on the right side of some images was caused by a faulty aperture. Figure 3-7 shows the same sample but with two additional images to show the evolution of the largest pit. ImageJ was used to measure the pit's growth during its first 45 s. This showed the pit growing downwards preferentially, this is likely caused by the released corrosion products falling downwards after they leave the pit. This can be seen visually by the dark streak shown at 1755 s.
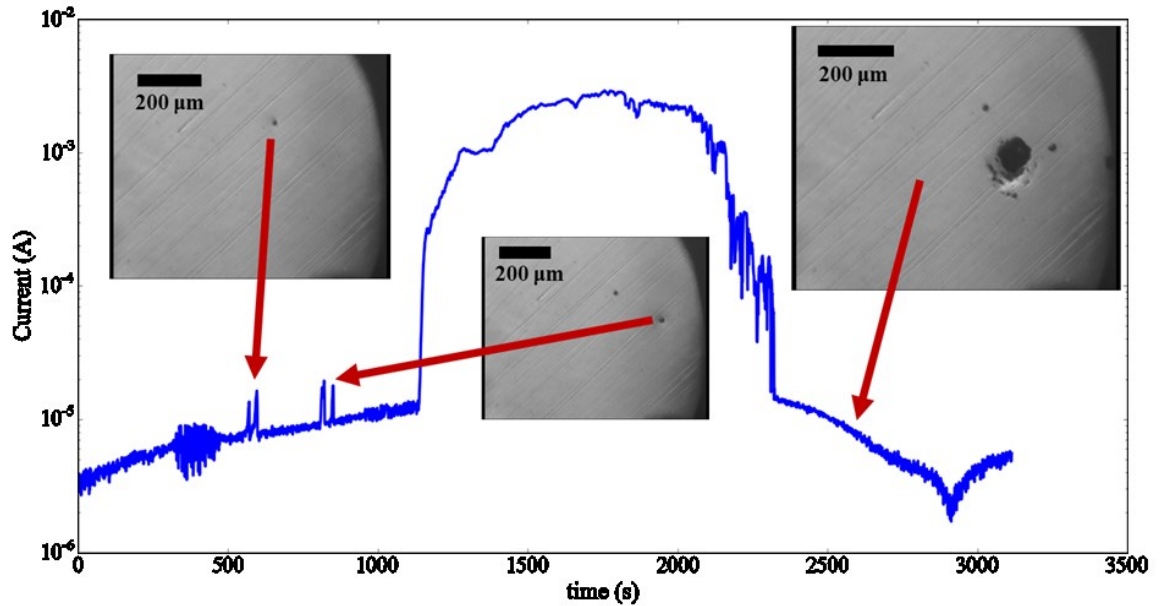
Figure 3-6:   Current-time graph showing how specific pitting events can be correlated with current spikes using optical microscopy videos.
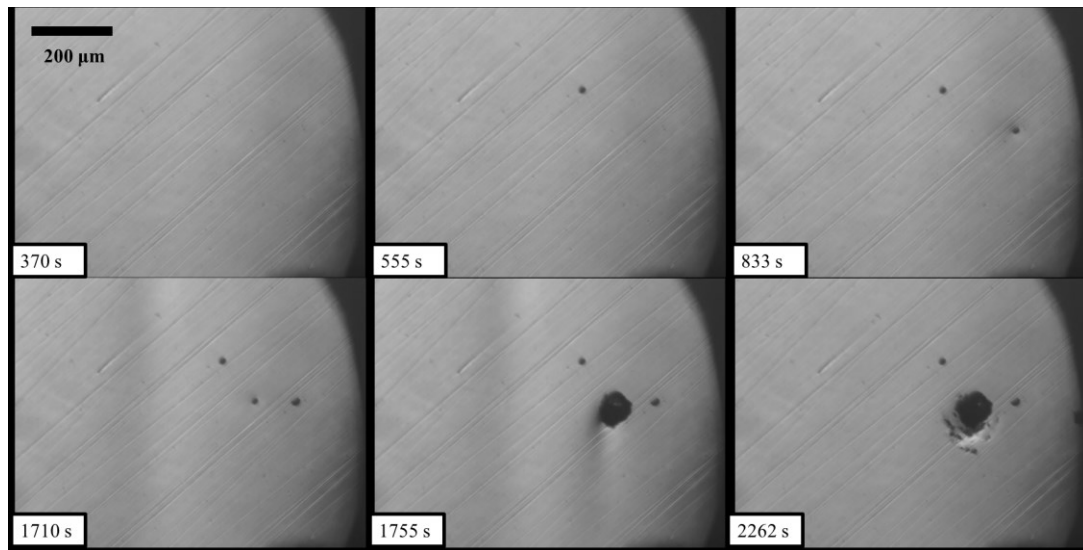
Figure 3-7:   Optical microscopy images for a water treated sample, tested on July 18, 2017. During the initial growth phase of the largest pit (between 1710 s and 1755 s) growth is highly anisotropic with the pit growing downwards at more than three times the speed as it was growing upwards (0.31 μm/s vs 1.02 μm/s). This was likely caused by the significant release of corrosion products which can be seen falling downwards in the image taken at 1755 s. Overall during the first 45 s of growth the large pit grew at a rate of 0.58 μm/s radially.

Some anomalous behaviour was observed during testing, for example Figure 3-8 shows microscope images of patterned corrosion occurring on a water treated sample. The corrosion occurs in a straight line, suggesting a scratch from polishing as the probable cause. Alternatively, this could be caused by an edge effect from the nail polish surrounding the sample where the nail polish being above the surface of the sample causes a crevice-like geometry. Some smaller pits are observed forming on the surface as well, for example one is indicated by the red arrow at 2335 s.
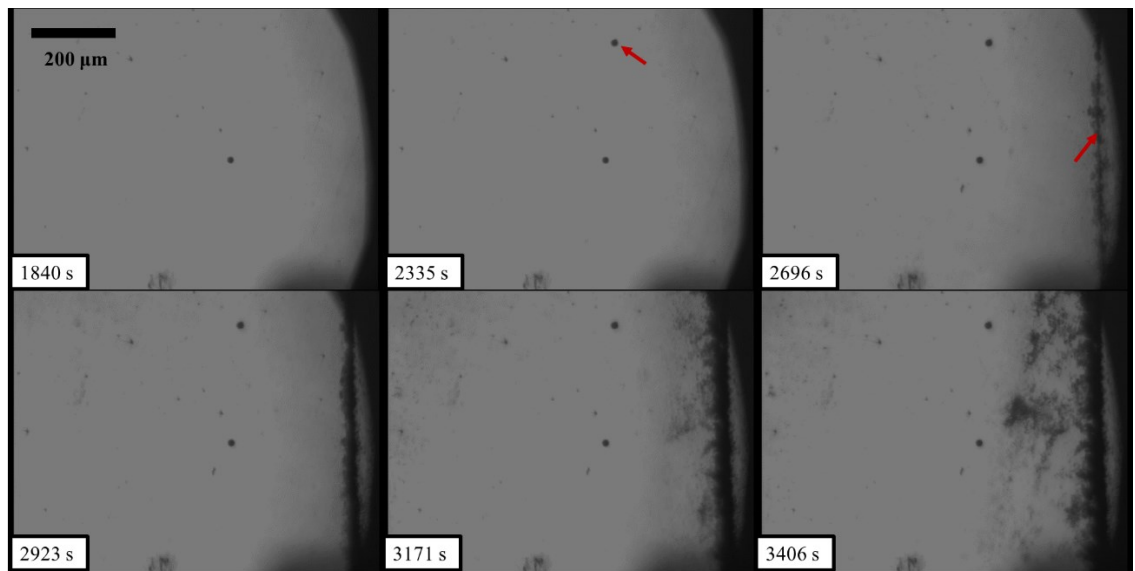
Figure 3-8:   Optical microscopy images for a water treated sample, tested on July 18, 2017. The first arrow shows normal pitting corrosion occurring, the second arrow highlights a form of patterned corrosion occurring along a straight line. Probably caused by a scratch in the sample surface.

Figure 3-9 shows the interesting corrosion behaviour observed in the heat treated samples. These microscope images have been brightened post measurement, because heat treated samples generally had lower reflectivity which is apparent in Figure 2-4. Heat treatment is expected to make a thicker, but lower quality oxide layer. This prediction

was confirmed with electrochemical testing showing that the heat treated samples had the lowest critical pitting potential as shown in Table 3-1. This finding was further complicated by Figure 3-4 which shows a qualitatively different curve shape for heat treated samples, where the current increases more slowly, in a similar manner to the water splitting region of other curves.

This might be explained by looking at Figure 3-9 which shows corrosion spreading primarily across the sample surface destroying the oxide layer and exposing fresh metal below. This spreading mechanism is similar to a growing mould, which spreads primarily across the surface. This is in contrast to the corrosion observed in samples from other surface treatments, which tended to eat into the metal in more localized pits. This generalized surface corrosion is best shown in Figure 3-9, where the corrosion starts at small holes in the oxide layer at approximately 285 s. The corrosion then spreads rapidly over the surface showing minimal sub-surface damage, between 285 s and 413 s corrosion spreads at an average rate of 0.33 µm/s radially, although this rate was highly variable with some areas expanding much faster. Areas where corrosion occurred more slowly tended to show greater surface damage. As an example the black area in the bottom left quadrant of the images, shows heavy surface damage, and also showed no expanding front of removed oxide. The oxide which was eventually removed around this area was destroyed by corrosion fronts from other areas.
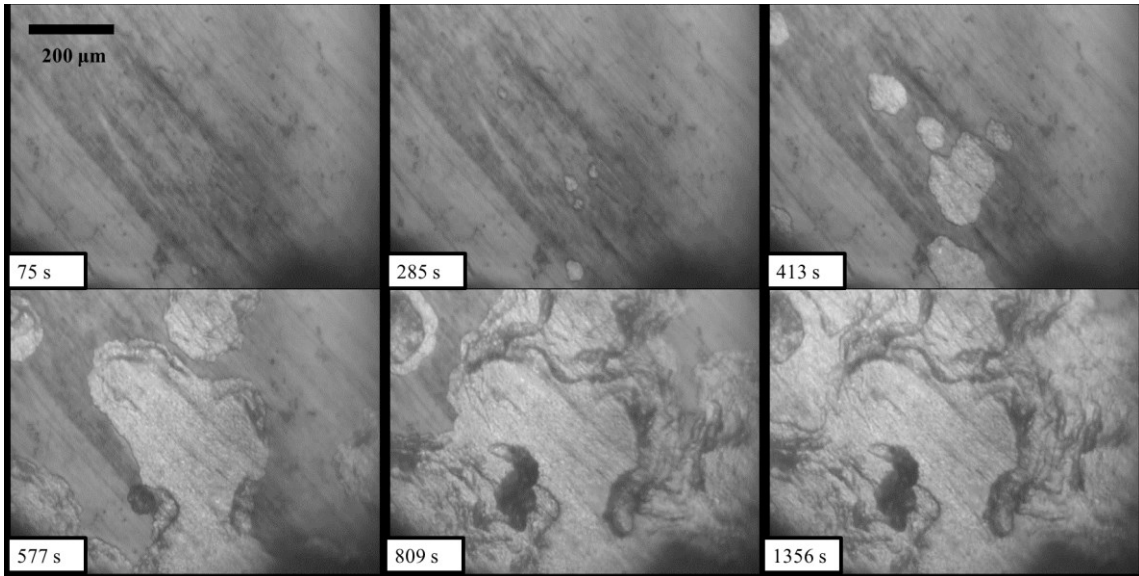
Figure 3-9:   Optical microscopy images of a heat treated sample, tested on December 27, 2017. Once the oxide layer breaks, the remainder of the oxide layer deteriorates very quickly. Also notice the relatively minor damage to the metal underneath the oxide layer, and very low reflectivity of the initial surface.

Figure 3-10 shows a different heat treated sample, where corrosion occurred under the oxide layer, but without a generalized breakdown as in Figure 3-9. This intact oxide layer forms a blister like morphology with corrosion products and electrolyte building up under the oxide layer. In this case it appears that corrosion was much more similar to normal metal samples where a pit first forms under the oxide layer by cation vacancy transport or oxide penetration. However, the pit formed was much larger than those observed on other surface treatments. Initially the blister grew at 0.30 μm/s between 530 s and 622 s. The pit then expands rapidly while keeping the oxide layer cap intact. Between 622 s and 679 s the blister grew at an average rate of 0.47 μm/s and between 679 s and 808 s it grew at 0.49 μm/s. Between 808 s and 1128 s the main blister ruptured, releasing corrosion products and leading to slower growth of only 0.22 μm/s,

47

this could likely be caused be the release of corrosion products leading to a more neutral environment inside the blister. The increased thickness of the heat treated oxide layer probably helped the blister stay intact for so much longer than in pitting corrosion observed on other samples, and would help explain the significant surface damage caused after the rupture. It is also likely that sub-microscopic pores formed in the oxide layer allowing electrolyte exchange. Similar pores were observed using SEM in several corroded SS316 wire samples.
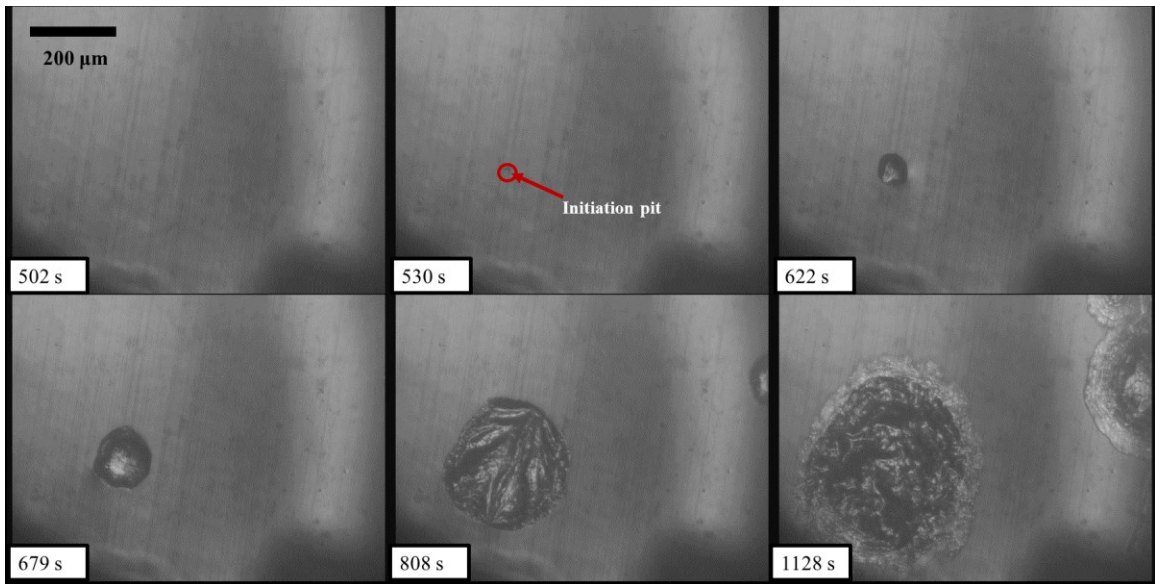
Figure 3-10: Optical microscopy images of a heat treated sample, tested on Dec 27, 2017. Corrosion happens under the oxide layer, in the video the oxide layer then begins to "flutter" much like the surface of a blister. The oxide layer eventually ruptures and the released corrosion products cause damage to the surface around the pit as shown in the last image.

Figure 3-11 shows how rapidly pits can grow. In this case a hydrogen peroxide treated sample is shown. During the first 20 s, pit growth is rapid and uniformly circular. Between 2262 s and 2269 s it grows at a rate of 1.21 µm/s, this slows to 0.87 µm/s between 2269 s and 2280 s and further slows to 0.39 µm/s between 2280 s and 2315 s.

After approximately one minute the pit begins to show anisotropic growth with some sections continuing to grow rapidly while other areas stop corroding entirely. Eventually satellite pits begin to form around the main pit. The exact mechanism is unknown, but previous papers have shown that released corrosion products lead to weakening of the oxide layer around the pit [37]. Figure 3-12 shows a proposed formation mechanism where the pit expands under the metal surface and satellite pits form by eating upwards from the main pit. The fact that the satellite pits preferentially formed below the initial pit, in an area where corrosion products had fallen earlier, lends credibility to the idea that corrosion products weakening the oxide layer help initiate corrosion, as shown in Figure 3-12 (B). These falling corrosion products can clearly be seen as a dark streak at 2315 s.
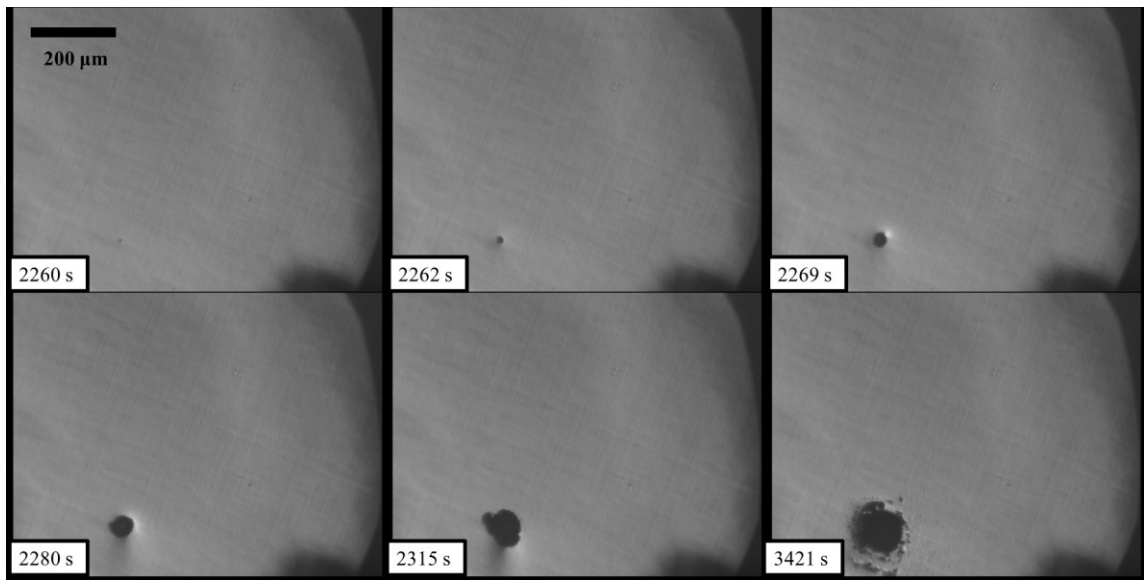
Figure 3-11:   Optical microscopy images of a hydrogen peroxide treated sample tested on August 2, 2017. The pit shows a very rapid increase in size during the first 20 s of corrosion. This is followed by slower and less circular growth in the final stages of corrosion.
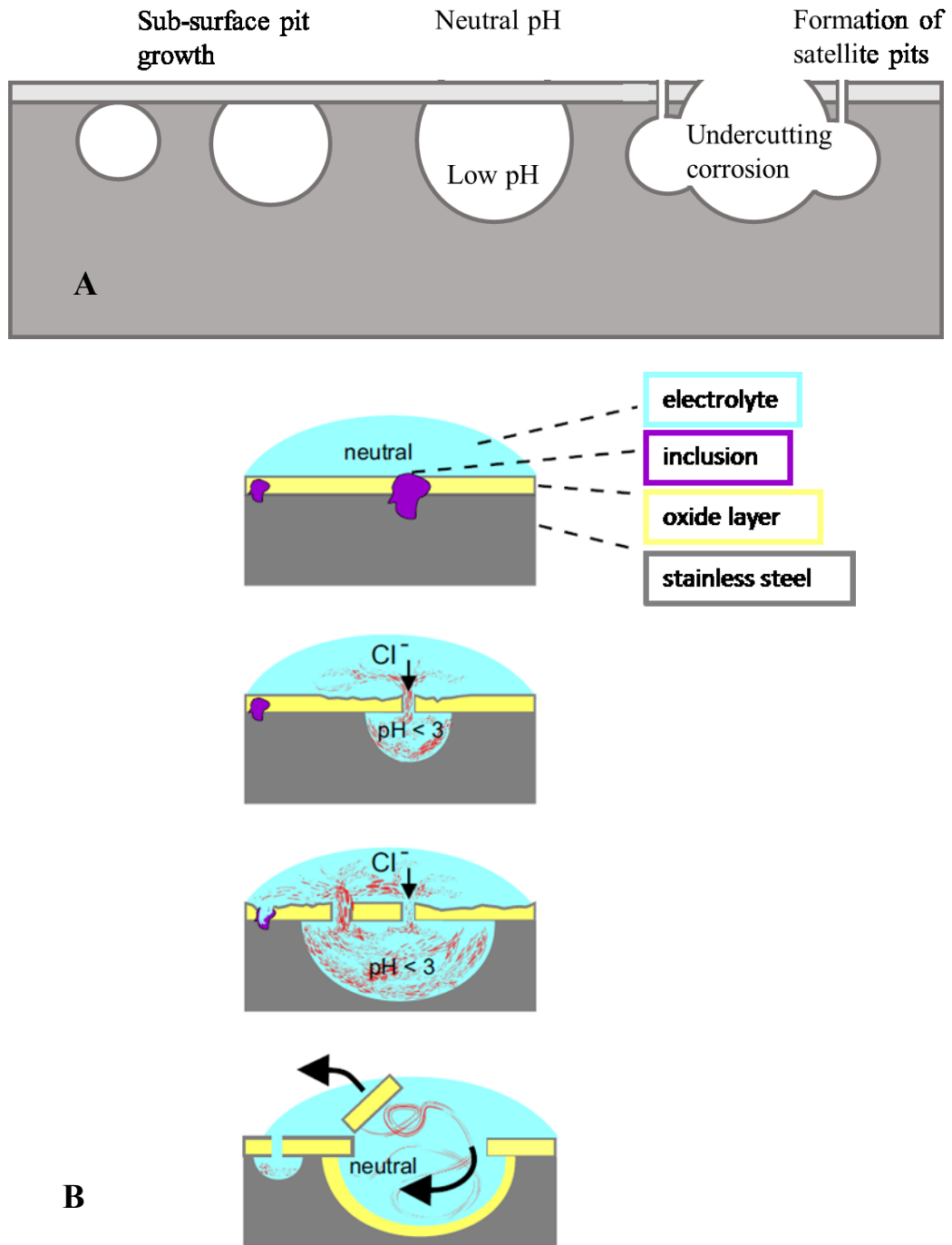
Figure 3-12: (A) proposed corrosion mechanism to explain undercutting corrosion, initial rapid growth and the formation of satellite peaks. Pit would be initiated by the penetration or cation vacancy transport mechanism. (B) mechanism showing how the release of corrosion products can lead to the weakening of the surrounding oxide layer [37].

3.2 X-Ray Photoelectron Spectroscopy

The Cr2p XPS spectra were fitted using a 3-peak model that accounted for the presence of chromium (III) oxide (Cr_2O_3) and chromium (III) hydroxide ($Cr(OH)_3$) as well as chromium metal (Cr(0)) which will be used later to estimate the oxide layer thickness. This model has been widely used to fit Cr2p peaks [8,38–43], but most of the fitting information to do with peak shapes and binding energies were taken from Biesinger, *et al* [34]. This was particularly important for the Cr(0) peak which uses an asymmetric peak shape made up of a superposition of 5 separate GL(30) symmetric peaks. All binding energies were verified using the National Institute of Standards and Technology (NIST) XPS database [44]. Specific information on all constraints used in this fit can be found in Appendix A, as well as tabulated values for the binding energies of all relevant chemical species. It is worth adding that some papers [45] added a fourth peak for chromium (VI) oxide (CrO_3) but this was not found to be necessary in this work.

Fitting Cr2p spectra can be simplified by only fitting the $2p_{3/2}$ peak. To show this is reasonable the untreated Cr2p spectrum was fitted for both peaks using a highly constrained copy of the $2p_{3/2}$ peaks. In this case area and full width half max (FWHM) were constrained to be equal to the values from the $Cr2p_{3/2}$ peak, while the peak position was given a small amount of freedom (±0.5 eV from the position predicted by spin-orbit splitting). The full fitted untreated Cr2p spectrum is shown in Figure 3-13. Figure 3-14 shows the same spectrum, with only the $Cr2p_{3/2}$ peak fitted to allow easier comparison with the other data. Data for the remaining surface treatments are shown in Figure 3-15-Figure 3-18. The heat treated Cr2p spectrum (Figure 3-17) showed unexpected

contamination by copper as shown by the Cu LMM peak. This was fitted and removed when determining compositions using an asymmetric peak.
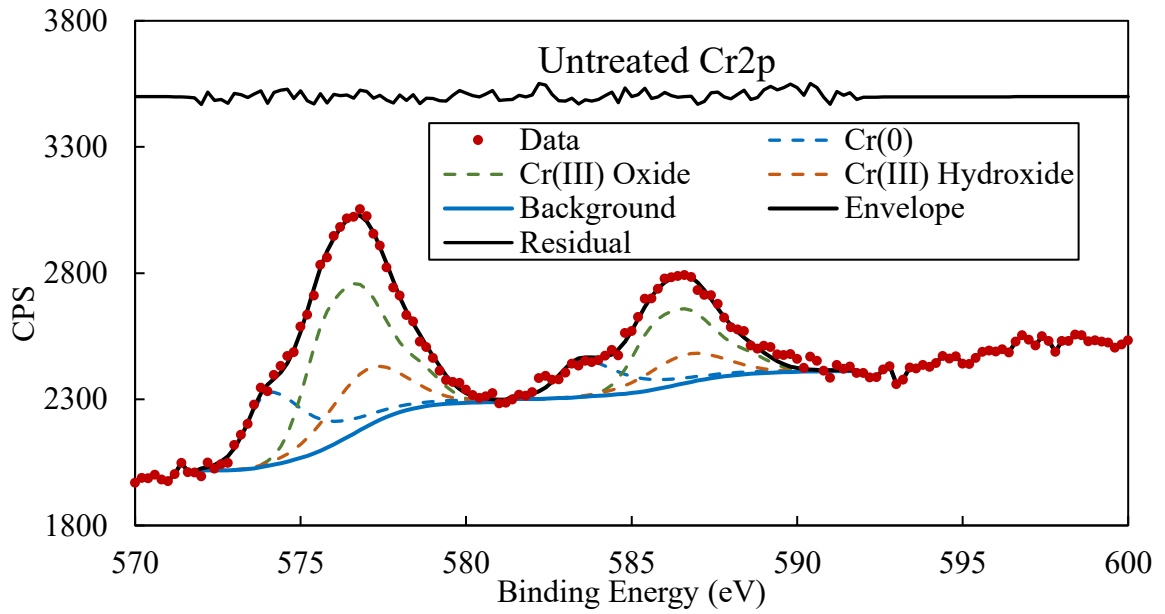
Figure 3-13:   Full Cr2p spectrum for untreated SS316. Fitted using a 3-peak model. Residual is small and relatively constant indicating a good fit. Detailed fitting parameters can be found in Appendix A.
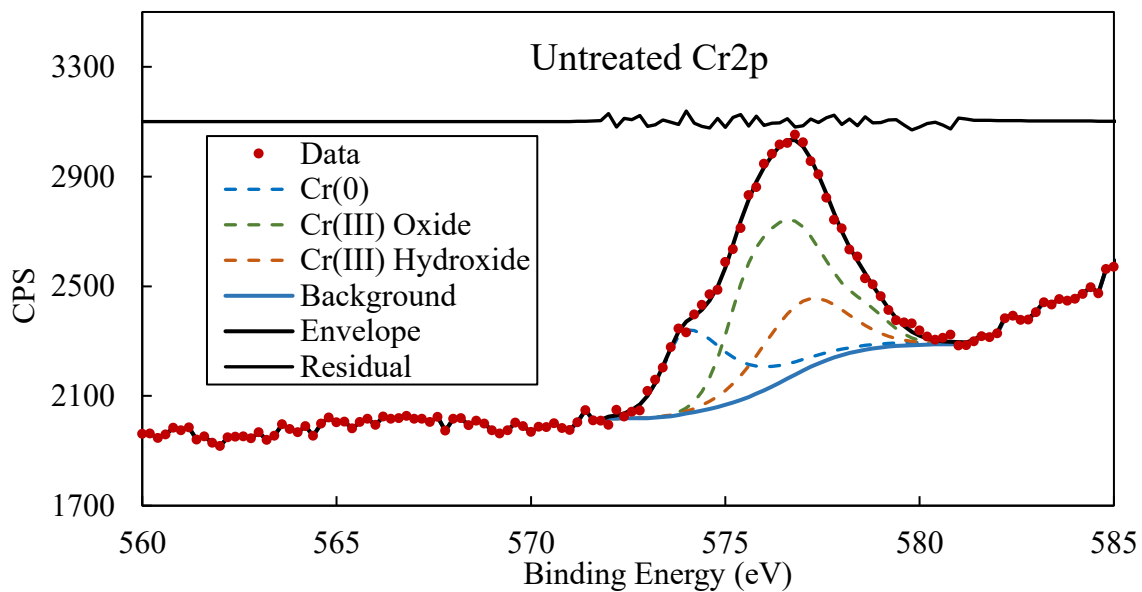
Figure 3-14: Cr2p$_{3/2}$ XPS peak for untreated SS316. Detailed fitting parameters and peak positions can be found in Appendix A.
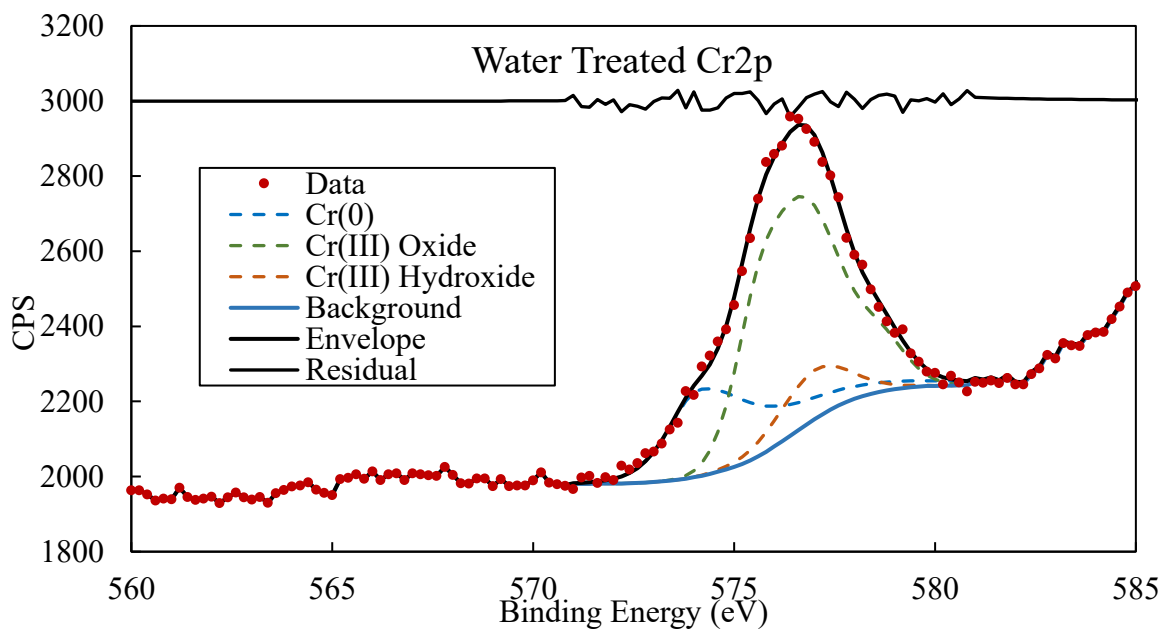
Figure 3-15: Cr2p$_{3/2}$ XPS peak for water treated SS316. Detailed fitting parameters and peak positions can be found in Appendix A.
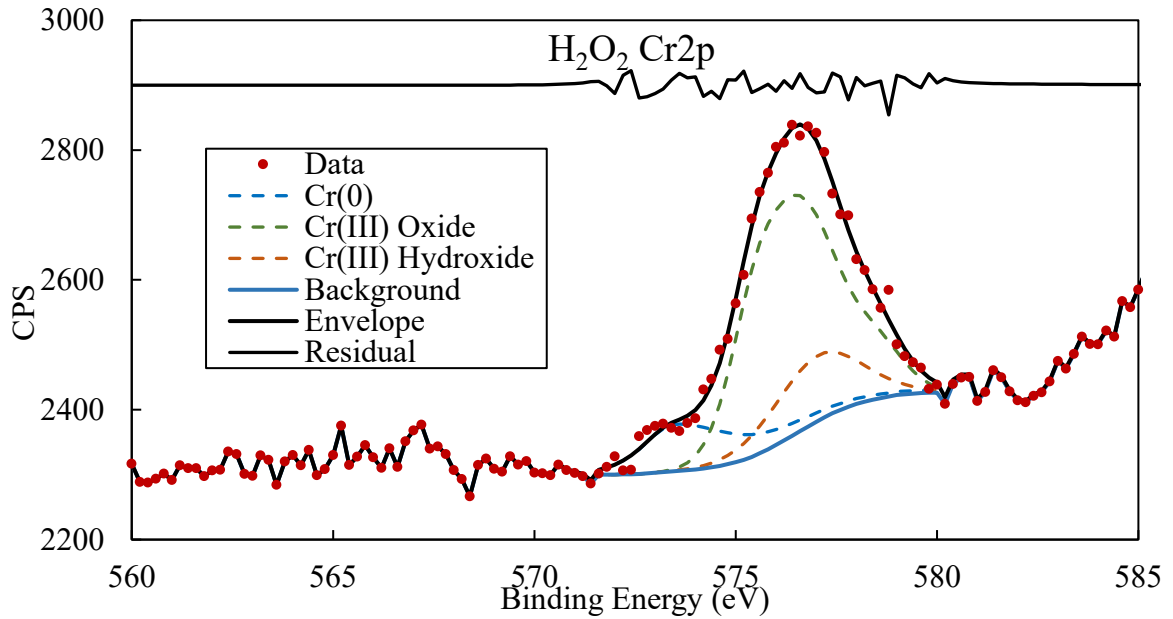
Figure 3-16:   Cr2p$_{3/2}$ XPS peak for H$_2$O$_2$ treated SS316. Detailed fitting parameters and peak positions can be found in Appendix A.
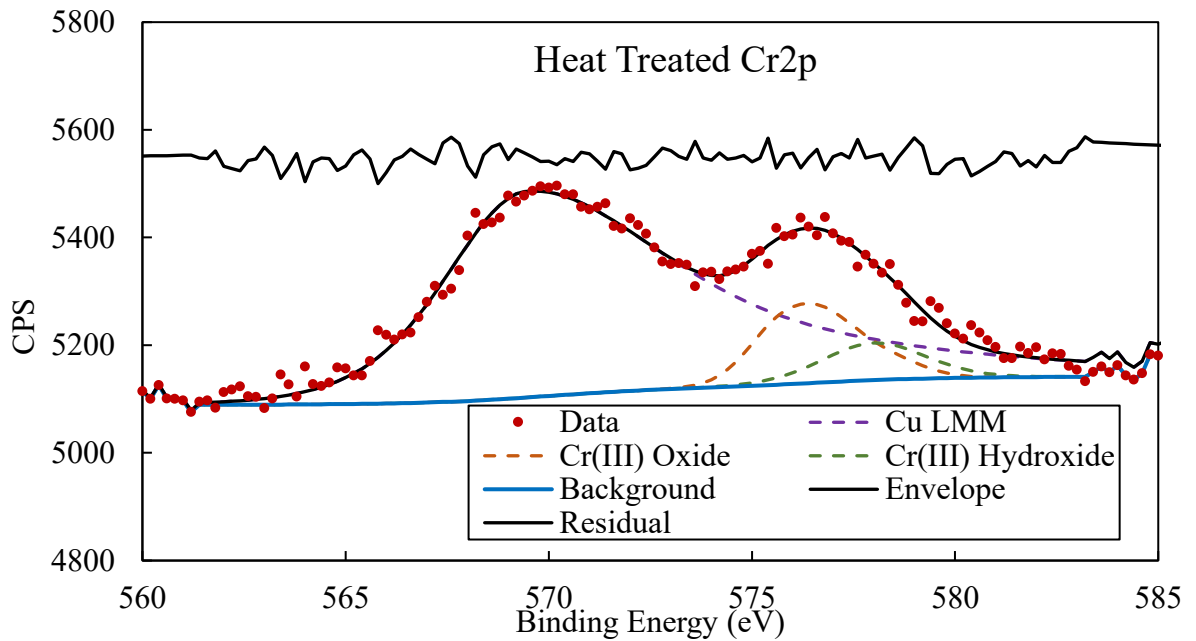
Figure 3-17:   Cr2p$_{3/2}$ XPS peak for heat treated SS316. This peak contained an unexpected Cu LMM peak which suggests contamination during the heat treatment process. Detailed fitting parameters and peak positions can be found in Appendix A.
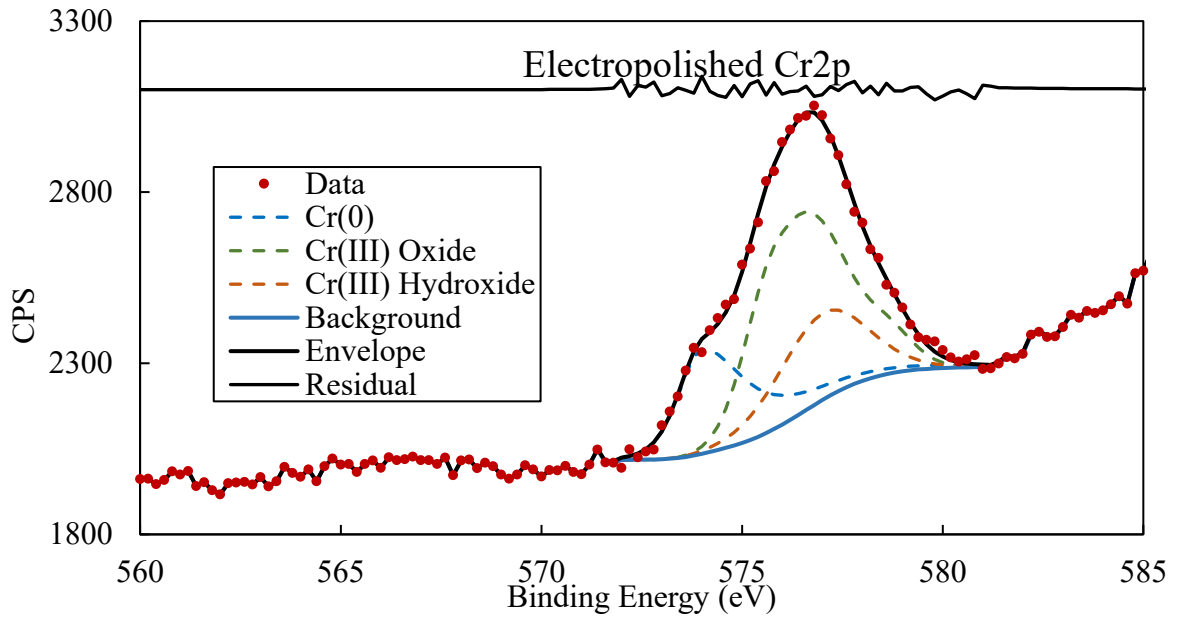
Figure 3-18: Cr2p$_{3/2}$ XPS peak for electropolished SS316. Detailed fitting parameters and peak positions can be found in Appendix A.

Fitting the O1s peak was done with an approximate model that uses only three peaks to represent a multitude of chemical species with very similar binding energies. This is illustrated in Table A-4, in Appendix A where five different oxides have binding energies within 0.5 eV. Nickel containing compounds show some more variation, with Ni_2O_3 having a binding energy similar to hydroxides, and $Ni(OH)O$ having a binding energy similar to oxides. In order to avoid fitting a spectrum with 10 different peaks, a simpler model was used to give the peaks more physical meaning. The third peak is used to fit water and organic species that are adsorbed onto the sample surface. Similar peak fitting techniques can be found in the literature [38–42,46], although some papers do attempt to fit with specific peaks for different chemical species [43]. The hydroxide peak is also attributed to imperfect oxides based on information in [34]. Fitted O1s peaks for all surface treatments are shown in Figure 3-19-Figure 3-23.
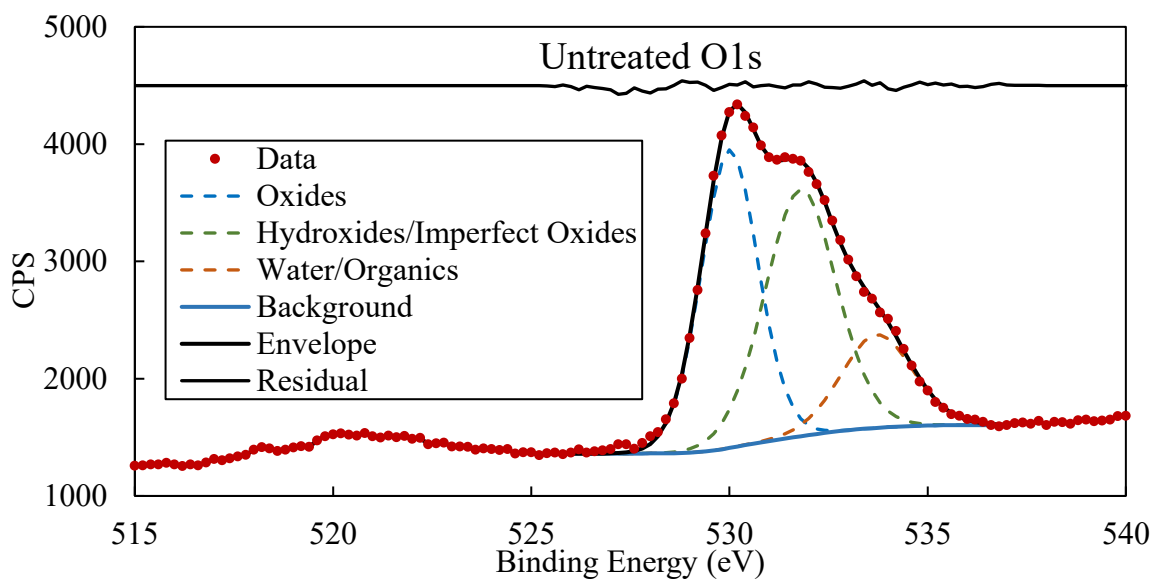
Figure 3-19: O1s XPS peak for untreated SS316. Note the large hydroxides/imperfect oxides peak on the right side of the peak. Detailed fitting parameters and peak positions can be found in Appendix A.
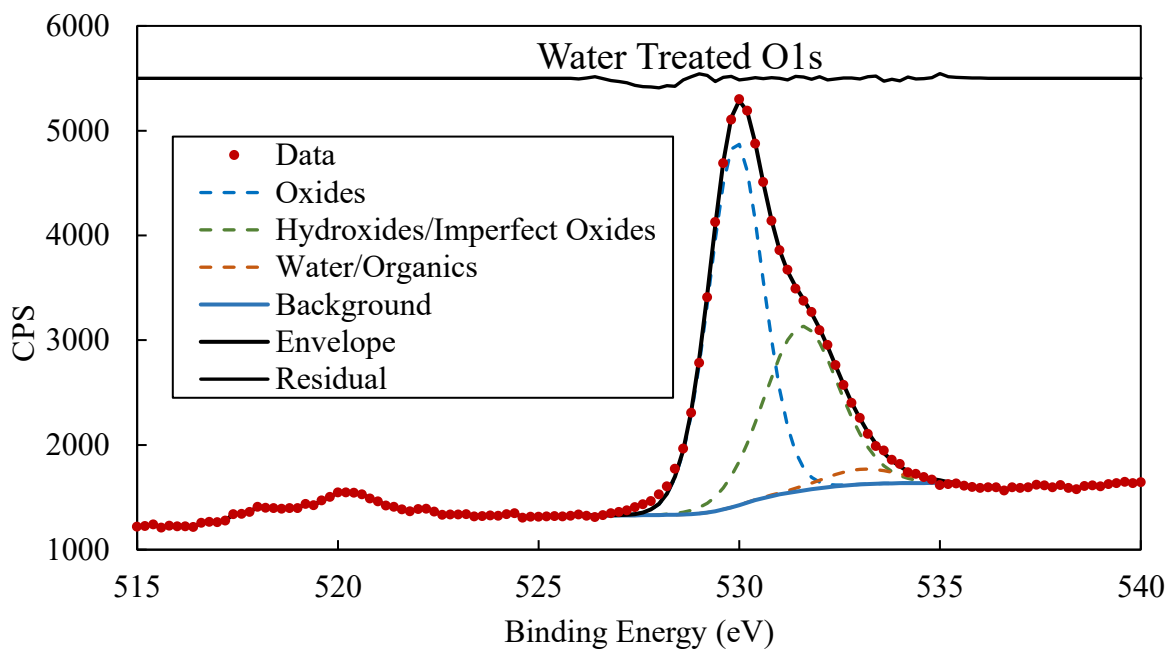
Figure 3-20: O1s XPS peak for water treated SS316. The fit slightly underestimates the data on the left side of the peak. Detailed fitting parameters and peak positions can be found in Appendix A.
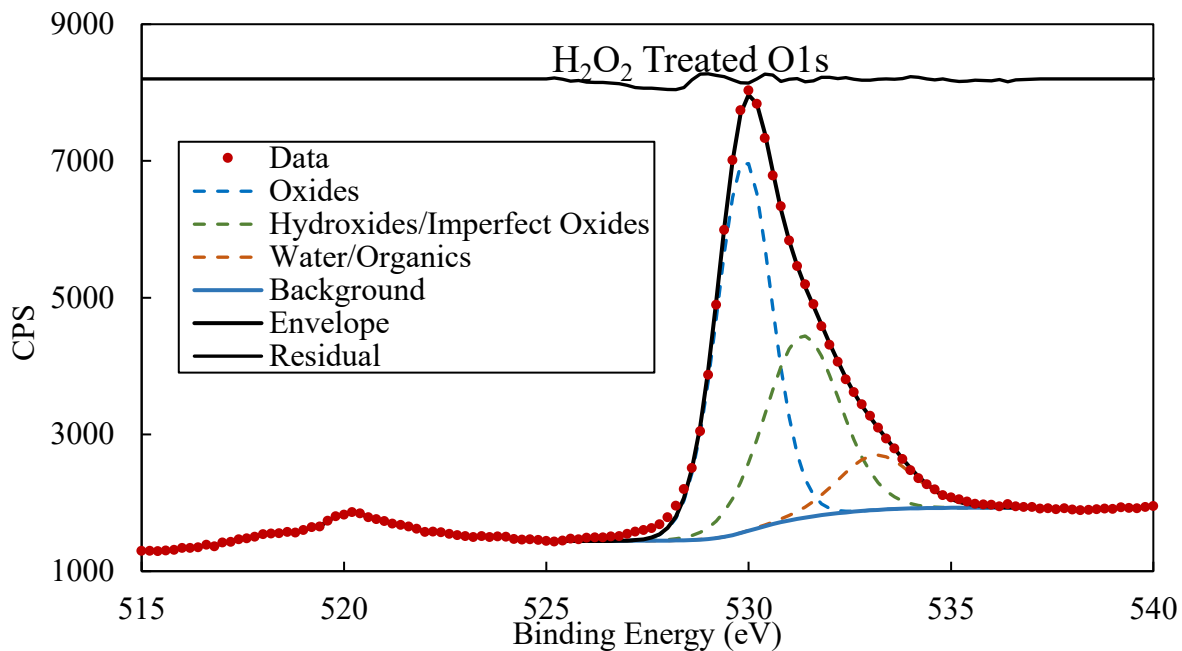
Figure 3-21:   O1s XPS peak for H_2O_2 treated SS316. Again the fit slightly underestimates the left side of the peak. Detailed fitting parameters and peak positions can be found in Appendix A.
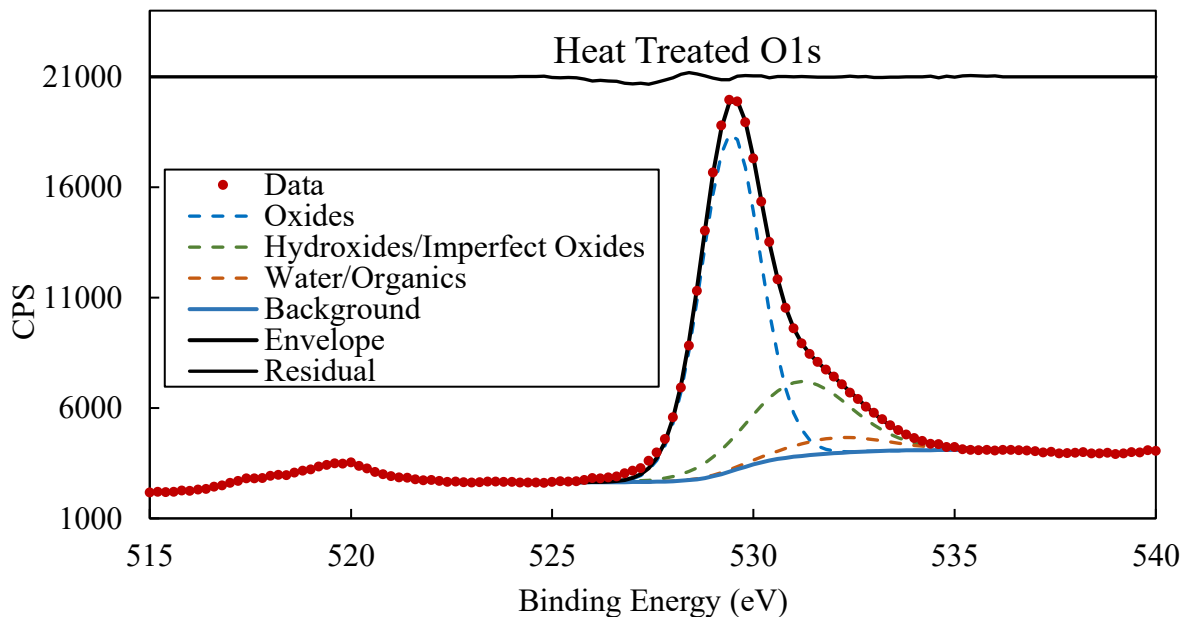
Figure 3-22:   O1s XPS peak for heat treated SS316. Detailed fitting parameters and peak positions can be found in Appendix A.
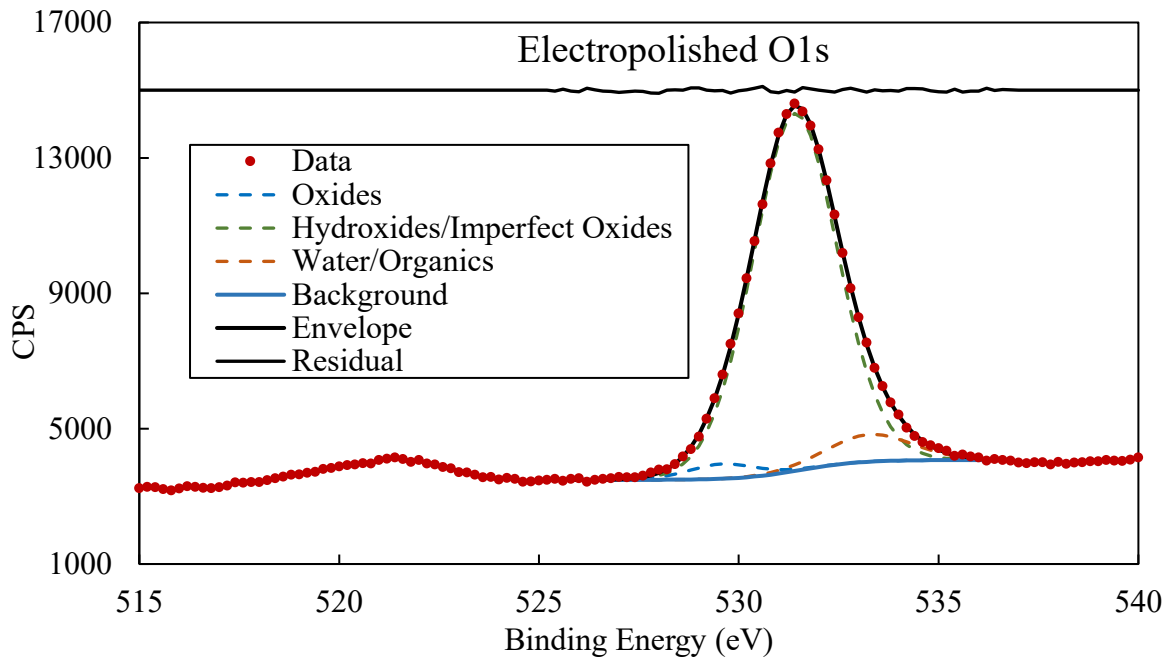
Figure 3-23:   O1s XPS peak for electropolished SS316. Detailed fitting parameters and peak positions can be found in Appendix A.

After fitting the XPS data using CasaXPS, composition data for the Cr2p and O1s peaks were determined. These are summarized in Table 3-3 and Table 3-4 respectively. Figure 3-25 and Figure 3-26 present the same data in a bar graph format. One aspect of the chemical composition that affects the corrosion resistance significantly is the ratio of the different types of Cr oxides and hydroxides. As shown in Table 3-3 both the water treated and hydrogen peroxide treated samples have a greater proportion of Cr oxides in their oxide layers compared to the untreated control. This shows that the hydrogen peroxide treatment achieved its intended effect of increasing the amount of oxygen available, leading to increased oxide formation. The enhanced amount of oxides present in the water treated samples was not an intended effect, but rather an unpredicted side-effect. A possible cause is the elevated temperature the treatment takes place at. Similar

effects are shown in a paper looking at the effect of a high temperature water treatment on a nickel based alloy [43].

Heat treated samples showed no Cr(0), which is probably caused by the significantly thicker oxide layer preventing measurement of the underlying bulk material. The thickness of the oxide layer was confirmed using ellipsometry to be on the order of 100 nm thick, much thicker than the measurement depth of XPS. Interestingly, the oxide to hydroxide ratio is lower than the untreated samples. A possible explanation is that the more rapid formation of the oxides leads to the formation of imperfect oxides, which are included in the hydroxides peak.

Electropolishing showed a significant enhancement in the amount of chromium hydroxide present. A similar effect was observed in a paper looking at electropolishing SS316 [8]. However, that paper showed a larger effect, possibly caused by electropolishing at a higher potential. A larger increase in the proportion of hydroxides was observed for the O1s peak, this would imply that Ni and Fe hydroxide species were enhanced more by electropolishing than Cr oxides.

An estimate of the oxide layer can be obtained by analyzing the amount of Cr(0) in the measured spectra. In a thicker oxide layer the amount of Cr(0) measured is expected to be lower. This can be calculated using the following equation [20]:

$$\frac{I_{A,\alpha}}{I_{B,\beta}} = \frac{I_{A,\alpha}^{\infty}}{I_{B,\beta}^{\infty}} \frac{\left(1 - e^{-d_A/\lambda(E\alpha)\cos\theta}\right)}{e^{-d_A/\lambda\left(E_\beta\right)\cos\theta}} \tag{8}$$

where $I_{A,\alpha}$ is the measured intensity due to the overlayer (in this case the oxide layer), $I_{B,\beta}$ is the measured intensity of the substrate, d_A is the thickness of the overlayer (in nm), $\lambda(E_\alpha)$ and $\lambda(E_\beta)$ are the electron inelastic mean free paths (IMFP) for the appropriate

kinetic energy (also in nm), θ is the electron takeoff angle relative to the surface normal (0° in this case). Finally $I^{\infty}_{A,\alpha}$ and $I^{\infty}_{A,\alpha}$ are the intensities due to A and B for infinite samples. By assuming that the intensities of infinite samples of oxide and Cr(0) are approximately equal the first term on the right hand side reduces to 1. Using the NIST Standard Reference 71 database, an IMFP of 1.407 nm is given for a kinetic of approximately 910 eV. Solving the simplified version of equation 8 and accounting for the takeoff angle gives the relatively simple result:

$$d_{oxide} = \lambda \ln \left(\frac{I_{oxide}}{I_{Cr(0)}} + 1 \right) \tag{9}$$

where d_{oxide} is the oxide layer thickness in nm, λ is the electron IMFP, I_{oxide} and $I_{Cr(0)}$ are the measured intensities due to oxides and the underlying metal respectively. The oxide layer thicknesses calculated from this equation are given in Table 3-2.
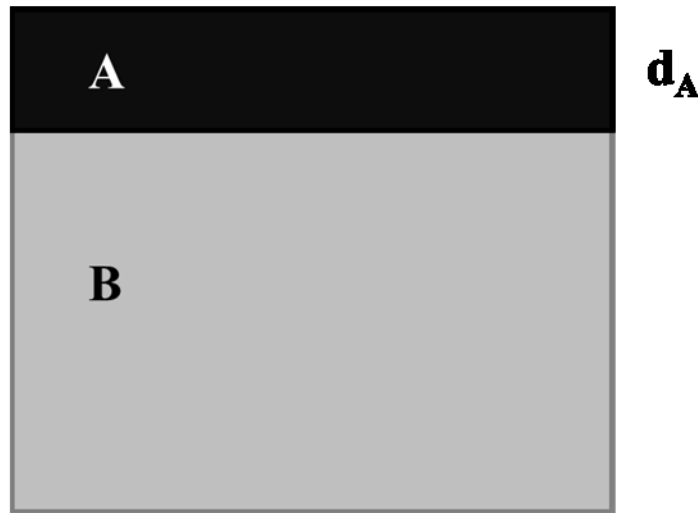
Figure 3-24: Schematic representation of the situation described by equation 8, with a thin overlayer A, of thickness d_A, on top of a substrate B.

Table 3-2:   Oxide layer thicknesses as estimated using the Cr2p XPS peaks for
             different treatments of SS316.

Treatment	Oxide Layer Thickness (nm)
Untreated	2.00
Water Treated	1.86
H_2O_2 Treated	2.62
Heat Treated	Too thick to estimate
Electropolished	2.04

Table 3-3:   Summary of chemical composition data derived from analysis of Cr2p
             peaks for the different surface treatments. Cr metal is expected because the
             XPS penetration depth of 3-4 nm is deeper than the oxide layer is thick, as
             determined by ellipsometry.

	% Cr (0)	% Cr (III) Oxide	% Cr (III) Hydroxide	Oxide to Hydroxide Ratio	Critical pitting potential (mV)
Untreated	24.1	54.1	21.7	2.49	640±70
Water Treated	26.7	63.4	9.9	6.40	770±50
H_2O_2 Treated	15.5	67.8	16.7	4.06	1390±40
Heat Treated	0	68.1	31.8	2.14	200±100
Electropolished	23.4	39.0	37.6	1.03	1050±80
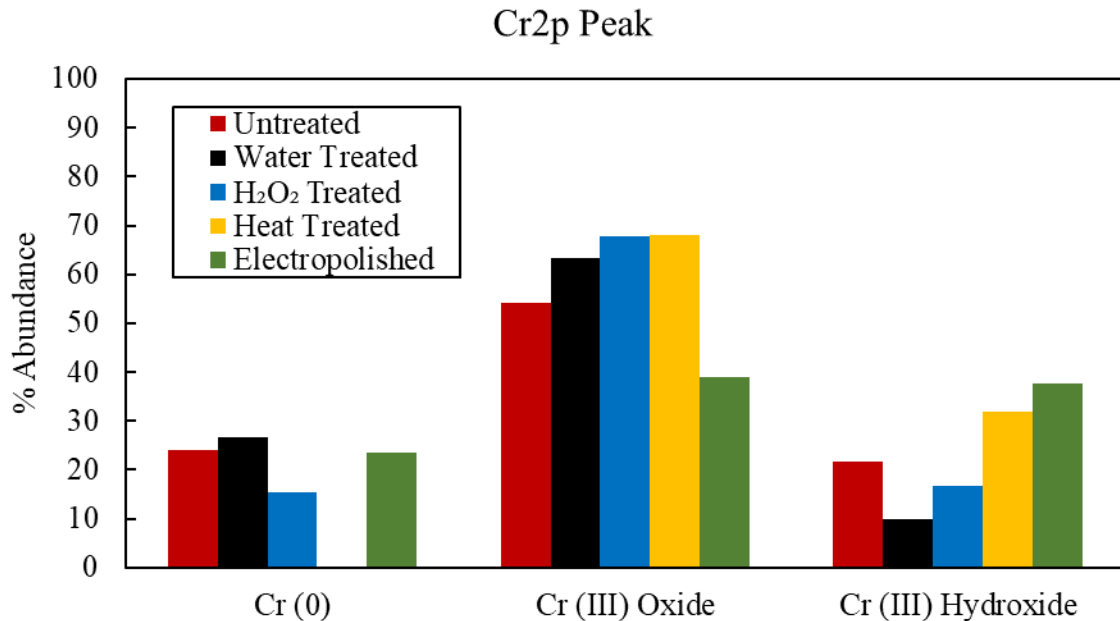
Figure 3-25:   Bar graph showing composition data for the Cr2p peak as determined by XPS.

The first thing apparent in Table 3-4 is that the oxide to hydroxide ratio is different to those given in Table 3-3. This is due to the results for the oxygen peak including other metal oxides and hydroxides such as those of Ni and Fe. The water and organic peaks are mostly representative of surface contamination from sample preparation and carbon monoxide deposition during XPS measurements. The oxygen peak confirms that water and hydrogen peroxide treatments increase the proportion of oxides relative to the untreated samples. The largest difference between the results for the Cr2p and O1s peaks is that the electropolished sample had very little signal from oxides in the O1s peak. This could be indicative of a greater proportion of nickel containing compounds in the electropolished oxide layer. As mentioned earlier an enhancement in the signal due to hydroxides is expected after electropolishing [8].

Table 3-4:   Summary of chemical composition data derived from analysis of O1s
peaks for the different surface treatments. The species used to fit these
peaks are more general and would include multiple chemical compounds
in each one.

	% Oxides	% Hydroxides/ Imperfect Oxides	% Organic/ Water	Oxides to Hydroxides Ratio
Untreated	41.1	42.8	16.1	0.96
Water Treated	59.6	37.0	3.4	1.61
H_2O_2 Treated	53.3	35.9	10.8	1.48
Heat Treated	68.8	25.9	5.3	2.66
Electropolished	3.0	90.2	6.8	0.03
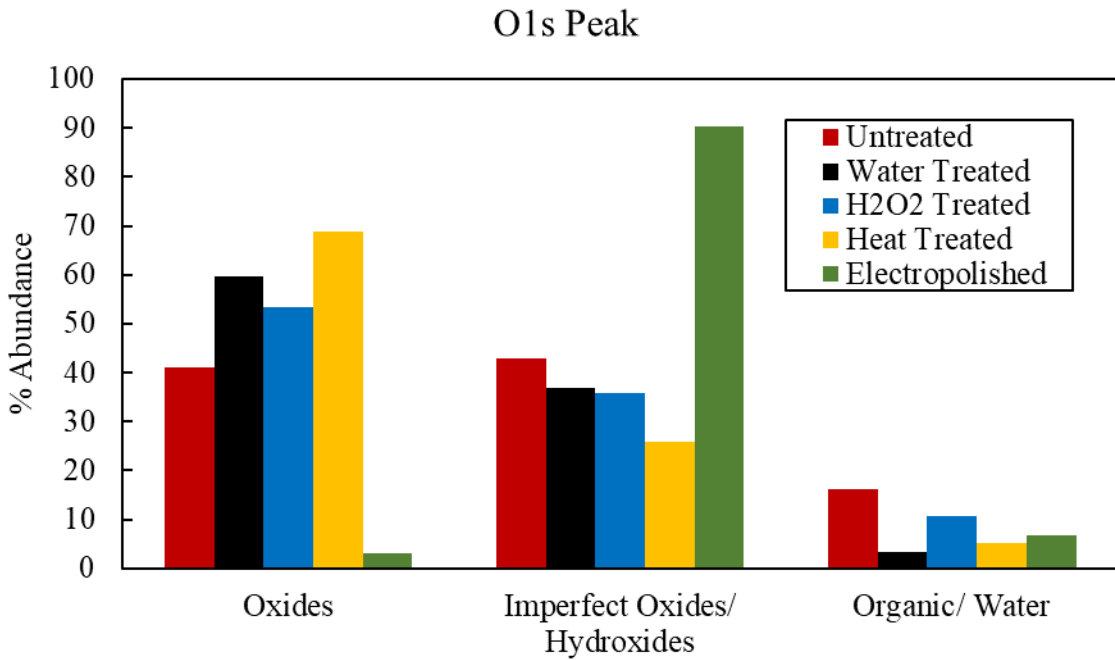
Figure 3-26:   Composition data from XPS for the O1s peak displayed as a bar graph.

3.3 Scanning Electron Microscopy

SEM images of all types of samples were taken post electrochemical testing. Figure 3-27 shows two different heat treated samples after corrosion testing. The thick oxide layer can clearly be seen peeling back in the first two images, while the third image shows "blistering" of the oxide layer probably caused by poor adhesion of the oxide layer and corrosion underneath the oxide layer creating pressure due to the build up of corrosion products.
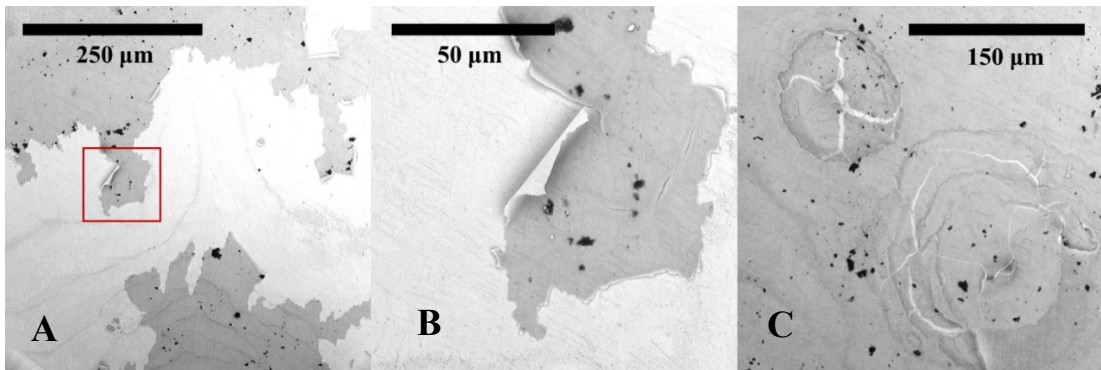
Figure 3-27: SEM images of a heat treated sample's surface, post testing. (A) illustrates how the oxide layer pealed away from the surface revealing fresh metal underneath (B) shows a detail from (A) indicated by the red box (C) shows what might be initiation sites for the breakdown of the oxide layer, appearing like blisters that developed under the oxide layer.

Cross section images of corroded stainless steel samples in Figure 3-28 can be used to confirm the geometry of corrosion pits. This illustrates the more rapid growth of corrosion pits under the surface as the acidic environment causes increased corrosion. It also illustrates how a cap made from the oxidized surface breaks away eventually to allow repassivation.

An unexpected morphology was observed in several wire sample cross sections, illustrated in Figure 3-29. After heavy corrosion, samples showed a layered morphology, with many small pores allowing electrolyte movement between the layers. It is important to consider that during testing the sides of the sample are covered with chemically inert Teflon™ and epoxy, so these pores are the only way for electrolyte to efficiently move between layers.
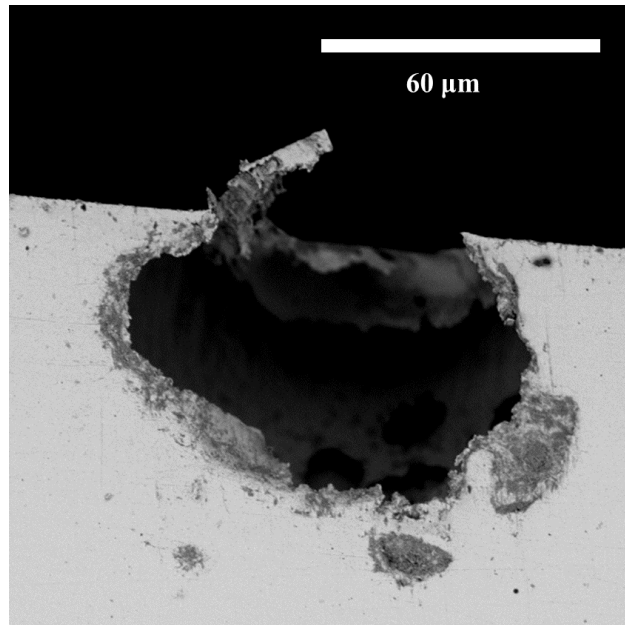
Figure 3-28:   SEM image showing the cross section of a pit formed in the polished face of an SS316 wire. Notice the still visible cap of the corrosion pit and undercutting corrosion. On the right side of the image damage from pit growth is visible as discoloration of the metal surface.
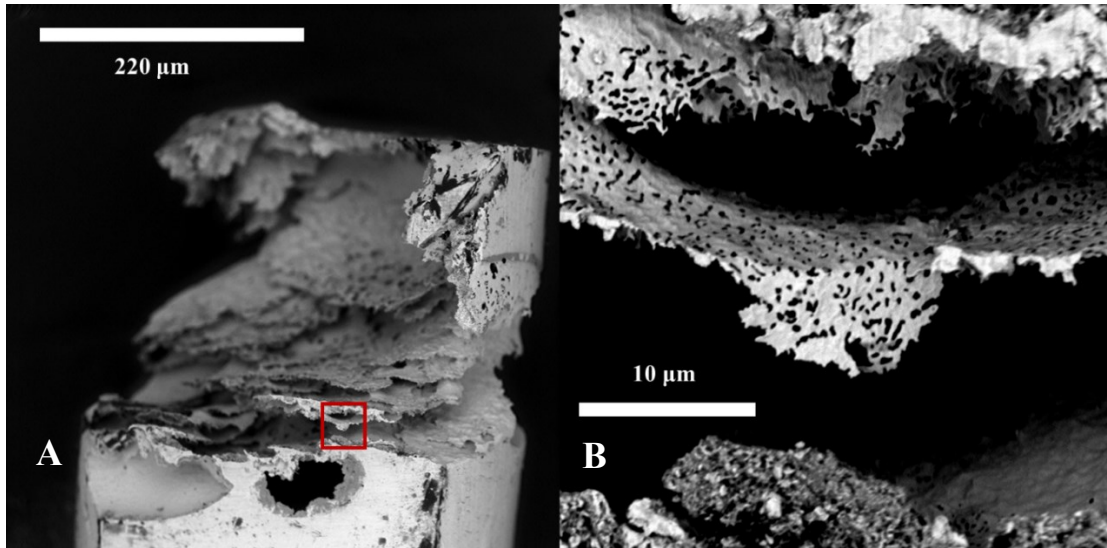
Figure 3-29:   SEM images showing the cross section of a heavily corroded SS316 wire sample. Detail shows the pores that form in thin layers of metal near corrosion. These would allow electrolyte exchange between pits and the sample surface.

SEM images of electropolished surfaces showed an etching effect caused by the polishing process, as shown in Figure 3-30. ImageJ software was used to measure the average size of the metal grains (measured along the long axis of grains). These measurements gave an average size of 26±1 μm, with a standard deviation of 8.7 μm for a total of 86 measured grains. Figure 3-31 shows three representative pits from an untreated SS316 sample, which clearly exhibit satellite pits forming around the central pit. This is solid evidence of corrosion pits expanding horizontally underneath the sample surface, undercutting the surface as shown in Figure 3-12. Unfortunately, orientation was not preserved when taking SEM images so it is impossible to determine if pits preferentially formed underneath the pits in these images. However, image (C) in Figure 3-31 shows relatively isotropic distribution of satellite pits, implying that at least in that case vertical orientation was not as important. Similar behaviour was observed in water treated and hydrogen peroxide treated samples, Figure 3-32 and Figure 3-33 respectively. The

66

sample shown in Figure 3-33 did not have the nail polish removed prior to SEM imaging to check if there was any evidence for preferential corrosion along the nail polish edge. The third image clearly shows a corrosion pit which is preferentially growing parallel to the nail polish edge. This suggests there are edge effects near the nail polish that make corrosion more favourable. This could potentially be a mild form of crevice corrosion, where the relatively tall nail polish edge prevents diffusion of electrolyte to the surface. For this reason, making the layer of nail polish thinner may reduce preferential corrosion near the sample edge.
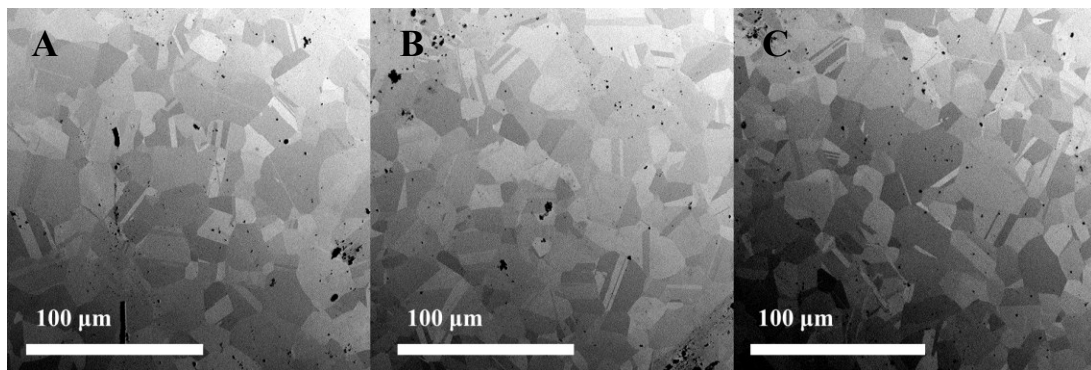
Figure 3-30:   SEM images of electropolished SS316 samples showing grain boundaries. Electropolishing's side-effect of etching the samples allowed for determination of the average grain size in the stainless steel samples using ImageJ.
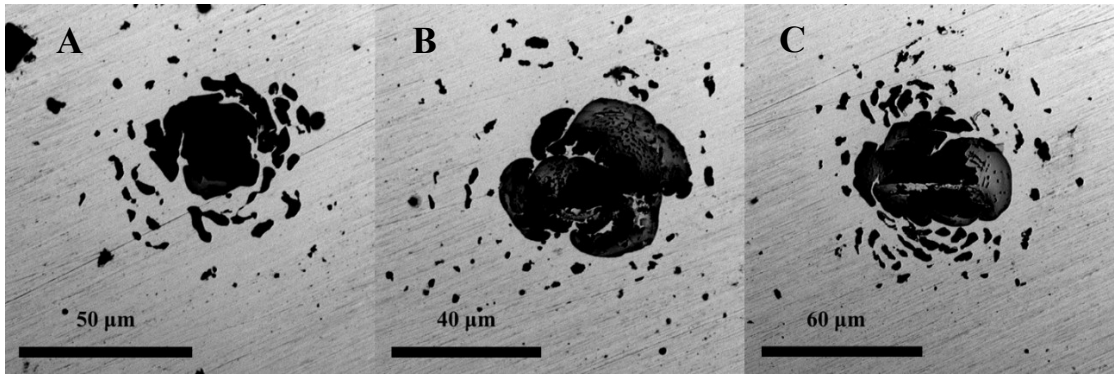
Figure 3-31:   SEM images of three representative corrosion pits taken from untreated
SS316 samples. Notice the concentric rings of satellite pits around the
main pits suggesting the pits undercut the metal surface.
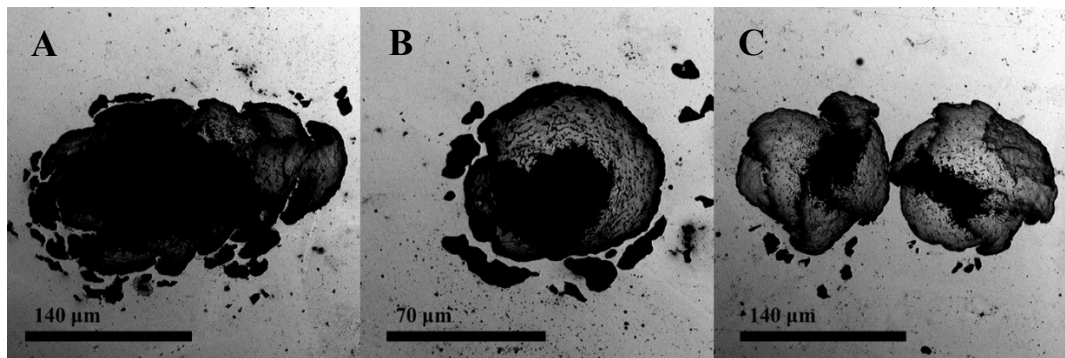
Figure 3-32:   SEM images of corrosion pits on water treated SS316. The first image (A)
shows an unusually elliptical pit, suggesting some sort of anisotropy in the
metal or a merger between two pits. (B) shows a typical pit, interestingly a
secondary surface is visible within the pit, and appears to show small
holes similar to those seen in Figure 3-29. The third image (C) shows two
twin pits that could potentially merge to form an elliptical pit.
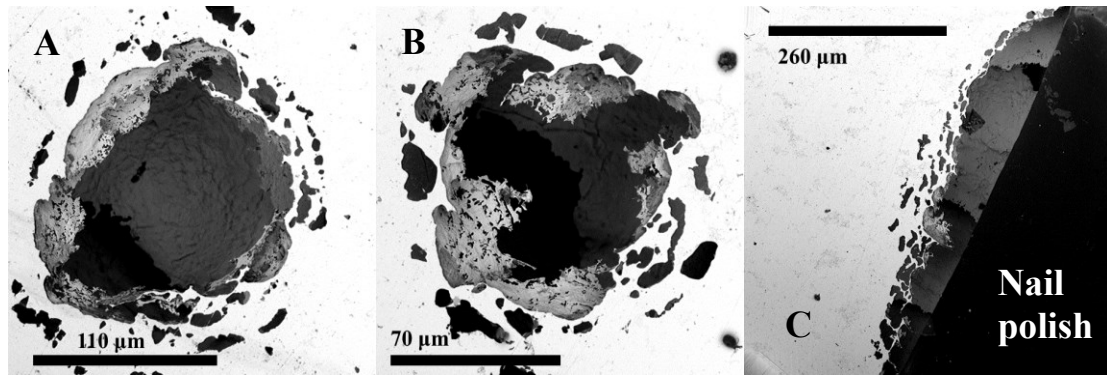
Figure 3-33:   (A) and (B) show SEM images of two corrosion pits on a hydrogen peroxide treated SS316 sample. Again satellite pits are around the main pit. The third image shows possible crevice corrosion near the edge of the nail polish covering. In this case the nail polish was left on the sample to look specifically for any corrosion that occurred near the edge of the sample.

Certain samples exhibited much more general corrosion, this is illustrated in Figure 3-34 for a hydrogen peroxide treated sample. This type of corrosion was most common in hydrogen peroxide treated samples as they had the highest critical pitting potentials, which meant that they spent the most time at high potential leading to more time to corrode. The first image in Figure 3-34 shows a very large corroded area which would release a large amount of corrosion products. The second image shows a closer view highlighting several things. First there is a secondary front showing an almost polished effect on the sample surface, and second the smaller pits that form before the main front tend to follow surface imperfections such as scratches in the sample surface.
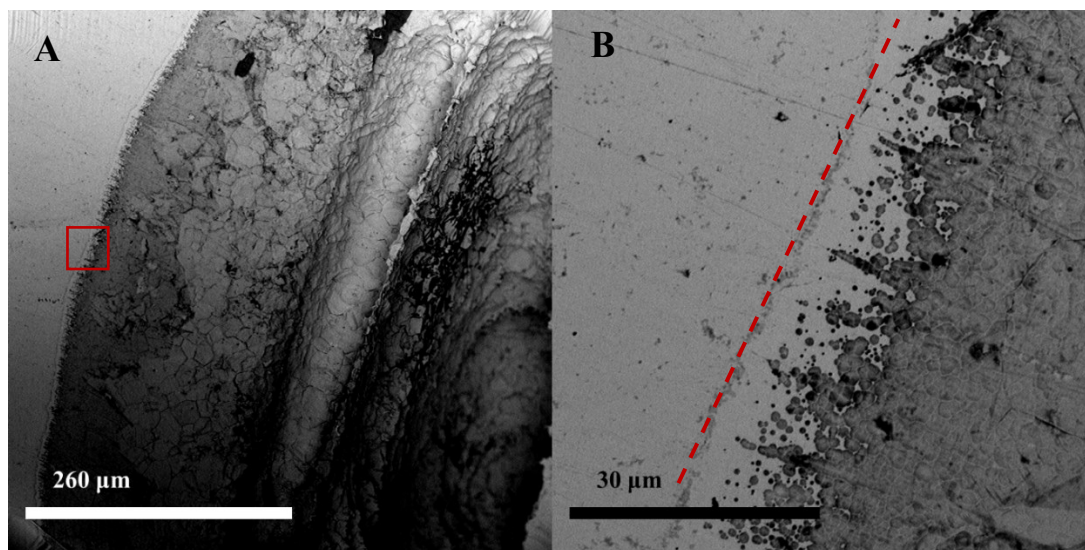
Figure 3-34: (A) SEM images of a hydrogen peroxide treated sample that exhibited widespread corrosion. The second image (B) shows a subsection of (A) indicated by the red square. This highlights smaller corrosion pits moving in front of the general front, and preferentially following scratches in the sample surface. The red dashed line in the second image highlights a secondary front that moves before the corrosion front, probably created by a more acidic environment near the area corroding.

3.4 Ellipsometry

Ellipsometry measurements and fitting were done by Leah Ellis on a single untested sample from each surface treatment. Untreated, water treated, and H_2O_2 treated samples all showed very consistent oxide layer thicknesses of 1.87 nm, 1.51 nm and 2.22±0.02 nm respectively. The heat treated sample showed a larger thickness of 76±2 nm. The electropolished sample was impossible to fit correctly, probably because of the less smooth finish.

These results show that there was not a significant change in the oxide layer thickness from the first three surface treatments. However, the heat treatment did significantly increase the oxide layer thickness, confirming what was observed under

SEM. These results also compare favourably with the estimations made based on XPS

results for the Cr2p spectra.

CHAPTER 4: CONCLUSION

All of the surface treatments tested in this work showed a positive effect on the corrosion resistance of SS316, except for the heat treatment. The greatest improvement in critical potential was observed for the hydrogen peroxide treatment. However, electropolishing showed the second best improvement while having significant advantages for treating objects with complex geometries. Despite electropolishing's practical advantages the tested treatments are advantageous for several reasons. Unlike electropolishing the water and hydrogen peroxide treatments are low cost and generate very little dangerous chemical waste. Both treatments are also similar to current sterilization techniques, and therefore could be incorporated into the maintenance of stainless steel medical instruments more easily. Further research is needed to determine their effectiveness on unpolished stainless steel, but this could be a useful application in treating stainless steel for applications that are not valuable enough to warrant electropolishing.

Optical and scanning electron microscopy were used to investigate the morphology and progression of corrosion. This showed that during pitting corrosion, satellite pits frequently formed around the original pit. In several samples preferential propagation below the pit was observed after corrosion products fell out of the pit. Heat treated samples showed different corrosion patterns, with either generalized breakdown of the oxide layer or the formation of blisters that were more akin to conventional corrosion pits.

XPS measurements were used to determine the chemical makeup of the various oxide layers. These measurements showed an increase in the amount of oxides for the water and hydrogen peroxide treatment, whereas electropolishing showed a large increase in the amount of hydroxides instead. Heat treatment was shown to make a much thicker oxide, with a large proportion of imperfect oxides. Copper contamination was also shown using XPS results. Finally, XPS measurements were used to estimate the oxide layer thickness and predicted a thickness of approximately 2 nm for all samples, except for the heat treated sample which had an oxide layer that was too thick to be measured estimated by XPS.

Ellipsometry measurements showed that there was no significant change in the thickness of oxide layers for water or hydrogen peroxide treated samples and showed consistent results with what would be expected from the literature and XPS results. The heat treated sample's oxide layer was shown to be significantly thicker. Although the electropolished sample's oxide layer was not able to be measured by ellipsometry it is reasonable to assume its thickness is approximately 2 nm, based on the XPS results' agreement with ellipsometry measurements.

REFERENCES

[1]   *Handbook of Stainless Steel*. Outokumpu Oyj, 2013.

[2]   H. M. Cobb, *The History of Stainless Steel.* Materials Park, OH: ASM International, 2010.

[3]   L. Karlsson, "Stainless steels: past, present and future," *Svetsaren,* vol. 47 no. 1 pp. 47-52, 2004.

[4]   E. McCafferty, *Introduction to Corrosion Science*. New York, NY: Springer Science & Business Media, 2010.

[5]   B. L. Bramfitt, J. R. Davis *Metals Handbook Desk Edition, Second Edition.* Materials Park, OH: ASM International, 1998.

[6]   K. Nomura and Y. Ujihira, "Analysis of oxide layers on stainless steel (304, and 316) by conversion electron Mössbauer spectrometry," *J. Mater. Sci.,* vol. 25, no. 3 pp. 1745-1750, 1990.

[7]   G. Manivasagam, D. Dhinasekaran and A. Rajamanickam, "Biomedical implants: Corrosion and its prevention – A review," *Recent Pat. Corros. Sci.*, vol. 2, no. 1, pp 40-54, 2010.

[8]   S. Habibzadeh, L. Li, D. Shum-Tim, E. C. Davis, and S. Omanovic, "Electrochemical polishing as a 316L stainless steel surface treatment method: Towards the improvement of biocompatibility," *Corros. Sci.,* vol. 87, pp. 89-100, 2014.

[9]   S. T. Kim and Y. S. Park, "Effects of copper and sulfur additions on machinability behaviour of high performance austenitic stainless steel," *Met. Mater. Int.,* vol. 15, no. 2 pp. 221-230 (2009).

[10]   N. Ånmark, A. Karasev, and P. G. Jönsson, "The effect of different non-metallic inclusions on the machinability of steels," *Materials*, vol. 8, pp 751-783, 2015.

[11]   D. E. Williams, M. R. Kilburn, J. Cliff, and G. I. N. Waterhouse, "Composition changes around sulphide inclusions in stainless steels, and implications for the initiation of pitting corrosion," *Corros. Sci.,* vol. 52, pp. 3702-3716, 2010.

[12]   A. Pardo, M. C. Merino, A. E. Coy, F. Viejo, R. Arrabal, and E. Matykina, "Pitting corrosion behaviour of austenitic stainless steels – combing effects of Mn and Mo additions," *Corros. Sci.,* vol. 50, no. 6, pp. 1796-1806, 2008.

[13]   J. Soltis, "Passivity breakdown, pit initiation and propagation of pits in metallic materials – Review," *Corros. Sci.,* vol. 90, pp. 5-22, 2015.

[14]   P. E. Klages, Z. Bai, M. Lobban, M. K. Rotermund, and H. H. Rotermund, "Enhancing resistance to pitting corrosion in mechanically polished stainless steel 316 LVM by water treatment," *Electrochem. Commun.,* vol. 15, no. 1, pp. 54-58, 2012.

[15]   M. P. Ryan, D. E. Williams, R. J. Chater, B. M. Hutton, and D. S. McPhail, "Why stainless steel corrodes," *Nature,* vol. 415, no. 6873, pp. 770-774, 2002.

[16]   T. L. S. L. Wijesinghe and D. J. Blackwood, "Real time pit initiation studies on stainless steels: The effect of sulphide inclusions," *Corros. Sci.,* vol. 49, no. 4, pp. 1755-1764, 2007.

[17]   "Manganese(II) sulfide safety data sheet," Sigma-Aldrich, 2017. Available at: https://www.sigmaaldrich.com/catalog/product/aldrich/400947, last accessed July 26, 2018.

[18]   G. O. Ilevbare, G. T. Burstein, "The role of alloyed molybdenum in the inhibition of pitting corrosion in stainless steels," *Corros. Sci.*, vol. 43, no. 3, pp. 485-513, 2001.

[19]   C. R. Clayton and Y. C. Lu, "A bipolar model of the passivity of stainless steel: The role of Mo addition," *J. Electrochem. Soc.*, vol. 133, no. 12, pp. 2465-2473, 1986.

[20]   D. Briggs and J. T. Grant, *Surface Analysis by Auger and X-Ray Photoelectron Spectroscopy*, Charlton, West Sussex, England: IMPublications, 2003.

[21]   C. R. Brundle, J. C. A. Evans, and S. Wilson, *Encyclopedia of Materials Characterization*, Stoneham, MA: Butterworth-Heinemann, 1992.

[22]   G. P. Williams, *Synchrotron Radiation*, National Synchrotron Light Source, Brookhaven National Laboratory, 1989.

[23]   "Inside the Synchrotron," Canadian Light Source. Available at: http://www.lightsource.ca/inside_the_synchrotron, last accessed August 23, 2018.

[24]   "XR3: Twin Anode X-ray Source," Thermo Scientific, 2008. Available at: https://static.thermoscientific.com/images/D16096~.pdf, last accessed July 26, 2018.

[25]   H. G. Tompkins and E. A. Irene, *Handbook of Ellipsometry,* Norwich, NY: William Andrew Publishing, 2005.

[26]   *NANOpure® DIamond™ Life Science (UV/UF): ultrapure water system operations manual*, Barnstead, Thermolyne, 2000.

[27]   J. L. Clayton, "A brief review of steam sterilization," *Periop Briefing*, vol. 106, no. 3, pp. 13-14, 2017.

[28] "Electropolishing vs passivation," ABLE Electropolishing, 2018. Available at: http://www.ableelectropolishing.com/resources/passivation-vs-electropolishing/, last accessed July 27, 2018.

[29] "Electropolishing of stainless steels," British Stainless Steel Association, 2018. Available at: https://www.bssa.org.uk/topics.php?article=131, last accessed July 27, 2018.

[30] S. A. Shabalovskaya, J. W. Anderegg, A. Undisz, M. Rettenmayr, and G. C. Rondelli, "Corrosion resistance, chemistry, and mechanical aspects of Nitinol surfaces formed in hydrogen peroxide solutions," *J. Biomed. Mater. Res. - Part B Appl. Biomater.* vol. 100, no. 6, pp. 1490-1499, 2012.

[31] "How to electropolish aluminum," Applied Science, 2014. Available at: https://www.youtube.com/watch?v=RVSB2Mo_PMY, last accessed August 20, 2018.

[32] V. Palmieri, "Fundamentals of electrochemistry – The electrolytic polishing of metals: Application to copper and niobium". *Proceedings of the 11th Workshop on RF-Superconductivity*, 2003.

[33] A. J. Bard and L. R. Faulkner, *Electrochemical Methods Fundamentals and Applications,* New York, NY: John Wiley & Sons, Inc., 2001.

[34] M. C. Biesinger, B. P. Payne, A. P. Grosvenor, L. W. M. Lau, A. R. Gerson, and R. S. C. Smart, "Resolving surface chemical states in XPS analysis of first row transition metals oxides and hydroxides: Cr, Mn, FE, Co and Ni," *Appl. Surf. Sci.,* vol. 257, no. 7, pp. 2717-2730, 2011.

[35] "Oxygen," Thermo Scientific XPS, 2018. Available at: https://xpssimplified.com/elements/oxygen.php, last accessed July 27, 2018.

[36] A. J. Bard and L. R. Faulkner, *Electrochemical Methods: Fundamentals and Applications.* New York, NY: John Wiley & Sons, 2001.

[37] C. Punckt, M. Bölscher, H. H. Rotermund, A. S. Mikhailov, L. Organ, N. Budiansky, J.r. Scully and J. L. Hudson, "Sudden onset of pitting corrosion on stainless steel as a critical phenomenon," *Science,* vol. 305, no. 5687, pp. 1133-1136, 2004.

[38] V. Maurice, W. P. Yang, and P. Marcus, "X-ray photoelectron spectroscopy and scanning tunneling microscopy study of passive films formed on (100) Fe-18Cr-13Ni single-crystal surfaces," *J. Electrochem. Soc.,* vol. 145, no. 3, pp. 909-920, 1998.

[39] I. Olefjord, and L. Wegrelius, "The influence of nitrogen on the passivation of stainless steels," *Corros. Sci.,* vol. 38, no. 7, pp. 1203-1220, 1996.

[40]   Z. Feng, X. Cheng, C. Dong, L. Xu, and X. Li, "Passivity of 316L stainless steel in borate buffer solution studied by Mott-Schottky analysis, atomic absorption spectrometry and x-ray photoelectron spectroscopy," *Corros. Sci.,* vol. 52, no. 11, pp. 3646-3653, 2010.

[41]   V. Maurice, W. P. Yang, and P. Marcus, "XPS and STM study of passive films formed on Fe-22Cr(110) single-crystal surfaces," *J. Electrochem. Soc.,* vol. 143, no. 4, pp. 1182-1200, 1996.

[42]   V. Maurice, W. P. Yang, and P. Marcus, "XPS and STM investigation of the passive film formed on Cr(110) single-crystal surfaces," *J. Electrochem. Soc.,* vol. 141, no. 11, pp. 3016-3027, 1994.

[43]   A. Machet, A. Galtayries, S. Zanna, L. Klein, V. Maurice, P. Jolivet, M. Foucault, P. Combrade, P. Scott, and P. Marcus, "XPS and STM study of the growth and structure of passive films in high temperature water on a nickel-base alloy," *Electrochim. Acta.*, vol. 49, pp. 3957-3964, 2004.

[44]   "NIST X-ray Photoelectron Spectroscopy Database", National Institute of Standards and Technology, 2012. Available at: https://srdata.nist.gov/xps/Default.aspx, last accessed August 23, 2018.

[45]   A. Kocijan, Č. Donik, and M. Jenko, "Electrochemical and XPS studies of the passive film formed on stainless steels in borate buffer and chloride solutions," *Corros. Sci.,* vol. 49, no. 5, pp. 2083-2098, 2007.

[46]   C. C. Shih, C. M. Shih, Y. Y. Su, L. H. J. Su, M. S. Chang, and S. J. Lin, "Effect of surface oxide properties of 316L stainless steel for biomedical applications," *Corros. Sci.*, vol. 46, no. 2, pp. 427-441, 2004.

APPENDIX A: XPS FITTING PARAMETERS

Table A-1:   Summary of all the constraints placed on the peaks used to fit the Cr2p peaks. The second half of this table shows constraints used to fit the Cr2p$_{1/2}$ peak which was only done for the untreated sample to show that fitting on the Cr2p$_{3/2}$ peak is sufficient. Peaks for the Cr2p$_{1/2}$ fit are highly constrained with only the peak position having a small amount of freedom, around the predicted position from spin-orbit splitting. Fitting parameters were primarily taken from [34].

	Peak Shape	Area Constraint	FWHM Constraint	Position Constraint
Cu LMM	LA(1.3, 4, 5)	n/a	0.72, 6	575, 565
Cr(0) "B"	LA(1.3, 4, 5)	n/a	0.72, 2	575, 573.5
Cr(III) Oxide "C"	GL(30)	n/a	0.2, 2	576, 575
Cr(III) Oxide Sat. 1	GL(30)	C*0.972	C*1	C+1.01
Cr(III) Oxide Sat. 2	GL(30)	C*0.528	C*1	C+1.79
Cr(III) Oxide Sat. 3	GL(30)	C*0.222	C*1	C+2.79
Cr(III) Oxide Sat. 4	GL(30)	C*0.139	C*1	C+3.2
Cr(III) Hydroxide "D"	GL(30)	n/a	0.2, 3	578, 577

	Peak Shape	Area Constraint	FWHM Constraint	Position Constraint
Cr(0)	LA(1.3, 4, 5)	B*0.5	B*1	584, 583
Cr(III) Oxide "E"	GL(30)	C*0.5	C*1	586, 585
Cr(III) Oxide Sat. 1	GL(30)	E*0.972	E*1	E+1.01
Cr(III) Oxide Sat. 2	GL(30)	E*0.528	E*1	E+1.79
Cr(III) Oxide Sat. 3	GL(30)	E*0.222	E*1	E+2.79
Cr(III) Oxide Sat. 4	GL(30)	E*0.139	E*1	E+3.2
Cr(III) Hydroxide	GL(30)	D*0.5	D*1	587.5, 586.5

Table A-2: Binding energy of different components in the Cr2p peaks. Binding energies for $2p_{3/2}$ and $2p_{1/2}$ peaks are given. Values were taken from the NIST XPS database [44].

Compound	$2p_{3/2}$ Binding Energy (eV)	$2p_{1/2}$ Binding Energy (eV)
Cr(0)	574.17	583.50
Cr_2O_3	576.65	586.15
$Cr(OH)_3$	577.22	586.80
CrO_3	579.24	No data found

Table A-3: Fitting constraints for the O1s peak, the relevant oxides and hydroxides for stainless steel are close together in binding energy so it is appropriate to fit the peak with more general peaks that represent groups of chemical compounds. Parameters were primarily taken from [35].

	Peak Shape	Area Constraint	FWHM Constraint	Position Constraint
Oxides	GL(30)	n/a	0.76, 2	530.5, 529.5
Hydroxides/ Imperfect Oxides "B"	GL(30)	n/a	0.76, 3	532, 531
Water/ Organics	GL(30)	n/a	B*1	533.5, 532

Table A-4: Binding energies for various possible oxides and hydroxides that could be found in the O1s peak. Values were taken from the NIST XPS database [44].

Compound	Binding Energy (eV)
Cr_2O_3	530.26
CrO_3	530.33
Fe_2O_3	530.00
FeO	529.95
Fe_3O_4	529.91
NiO	529.68
Ni_2O_3	531.60
$Cr(OH)_3$	531.33
$Cr(OH)O$	531.30
$Fe(OH)_3$	531.30
$Fe(OH)O$	530.74
$Ni(OH)_2$	531.27
$Ni(OH)O$	529.85